9

Review article

Michele Cotrufo, Liuyang Sun, Junho Choi, Andrea Alù* and Xiaoqin Li*

Enhancing functionalities of atomically thin semiconductors with plasmonic nanostructures

https://doi.org/10.1515/nanoph-2018-0185 Received October 31, 2018; revised February 19, 2019; accepted February 22, 2019

Abstract: Atomically thin, two-dimensional, transitionmetal dichalcogenide (TMD) monolayers have recently emerged as a versatile platform for optoelectronics. Their appeal stems from a tunable direct bandgap in the visible and near-infrared regions, the ability to enable strong coupling to light, and the unique opportunity to address the valley degree of freedom over atomically thin layers. Additionally, monolayer TMDs can host defect-bound localized excitons that behave as singlephoton emitters, opening exciting avenues for highly integrated 2D quantum photonic circuitry. By introducing plasmonic nanostructures and metasurfaces, one may effectively enhance light harvesting, direct valleypolarized emission, and route valley index. This review article focuses on these critical aspects to develop integrated photonic and valleytronic applications by exploiting exciton-plasmon coupling over a new hybrid material platform.

Keywords: exciton–plasmon coupling; metasurface; single-photon emission; TMD; valley polarization.

Michele Cotrufo: Department of Electrical and Computer
Engineering, The University of Texas at Austin, Austin, TX 78712,
USA; and Photonics Initiative, Advanced Science Research Center,
City University of New York, NY 10031, USA
Liuyang Sun and Junho Choi: Department of Physics, Complex
Quantum Systems, and Texas Materials Institutes, The University of

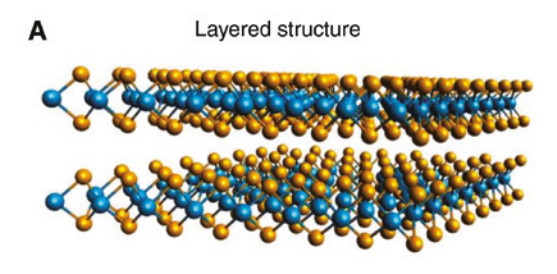
Texas at Austin, Austin, TX 78712, USA

1 Introduction

Two-dimensional semiconductors have attracted much interest in the last decade as a new material platform for valleytronics and optoelectronics [1-4]. Particular attention has been devoted to monolayer (ML) transition-metal dichalcogenides (TMDs), which are formed by a layer of transition-metal atoms [such as molybdenum (Mo) and tungsten (W)] sandwiched between two layers of chalcogenide atoms [such as sulfur (S) and selenium (Se)], with the metal and chalcogen atoms occupying the A and B sites of a hexagonal lattice (Figure 1). Exciton resonances in Mo- and W-family materials exhibit distinct optical properties because of their different spin orientations in the lowest conduction bands. In Mo-based TMD monolayers, the lowest exciton resonance is a dipole-allowed transition, while this transition corresponds to dark excitons in W-based TMD monolayers [5, 6]. These materials feature a combination of unique optical properties. Their electronic bandgap lies in the visible and infrared, and as the layer thickness is reduced, the electronic band structure changes significantly [7, 8]. In some TMD materials (e.g. MoS₂), an indirect-to-direct gap transition occurs when a bilayer is thinned down to a monolayer [9-11], thus strongly enhancing light emission and absorption in the MLs.

Mobile excitons in TMD monolayers exhibit large binding energy and oscillator strength, leading to strong resonant coupling to light [12–17]. In addition to mobile excitons, ML TMDs can also host localized excitons that are bound to the defects and behave as spectrally narrow single-photon emitters [18-20]. These localized emission centers often appear at the ML edges, but they can also be created or enhanced at specific positions by locally engineering the strain. Moreover, excitons form at the K and K' points located at the Brillouin zone boundary. Because of the broken inversion symmetry of the ML and the strong spin-orbit coupling, the electronic states of the two K and K' valleys have opposite spins, leading to spinvalley locking [21–23]. Because of the valley-contrasting optical selection rule, the valley index can be addressed and manipulated by light. Optoelectronic applications

^{*}Corresponding authors: Andrea Alù, Photonics Initiative, Advanced Science Research Center, City University of New York, NY 10031, USA; Physics Program, Graduate Center, City University of New York, NY 10016, USA; and Department of Electrical Engineering, City College of The City University of New York, NY 10031, USA, e-mail: aalu@gc.cuny.edu; and Xiaoqin Li, Department of Physics, Complex Quantum Systems, and Texas Materials Institutes, The University of Texas at Austin, Austin, TX 78712, USA, e-mail: elaineli@physics.utexas.edu. https://orcid.org/0000-0002-2279-3078



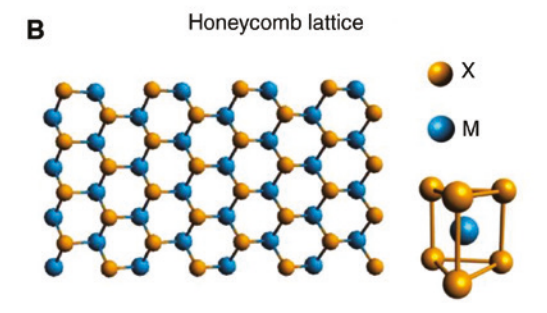


Figure 1: Atomic structure of TMDs.

(A) Three-dimensional schematic of a layered MX_2 (M = Mo, W; X = S, Se, Te) structure. In a TMD monolayer, a layer of transition metal atoms (M, blue spheres) is sandwiched between two layers of chalcogen atoms (X, yellow spheres). (B) Top and side views of a honeycomb lattice of a TMD with two sublattice sites occupied by metal and chalcogen atoms, respectively.

of TMDs are often limited by their low quantum yield. Improving the quantum yield of TMD monolayers remains therefore an active and important area of research [24, 25]. Additionally, light emitted from mobile or localized excitons needs to be efficiently collected and properly routed on chip for any integrated application.

In this review, we discuss how plasmonic nanostructures are particularly well suited for enhancing the optical properties of TMD MLs. Because of their two-dimensional nature, TMD MLs can be positioned very close, and optimally aligned, to a metallic structure. We have chosen to focus on emerging new directions in controlling a single emitter and valley index using plasmonic structures, and we anticipate rapid developments in these areas in the next few years. Because of the vast body of literature on TMD monolayers and many excellent reviews, we have omitted several interesting topics, including light-matter interaction in the strong coupling regime leading to the formation of polaritons [17, 26]. In Section 2, we briefly summarize the optical properties of TMD monolayers and the use of plasmonic nanostructures to control spontaneous emissions. In Section 3, we discuss different approaches to increase emission from mobile or localized excitons into either free space (mediated by plasmonic antennas) or plasmonic waveguides for on-chip propagation. In Section 4, we focus on recent experiments where the chirality of plasmonic fields is combined with the valley-selective response of TMD materials to increase valley polarization, direct valley-selective emissions, and a spatially separate valley index by exploiting exciton—plasmon coupling.

2 Basic concepts

2.1 Excitons in TMD monolayers

Excitons in TMD monolayers have several unique properties, including a small Bohr radius as well as large binding energy and oscillator strength [12–16]. Assuming a simple hydrogenic model, the *n*th exciton resonance binding energy in 2D materials is determined by

$$E_b^{(n)} = \frac{\mu e^4}{2\hbar^2 \varepsilon^2 (n-1/2)^2},$$

where μ is the reduced mass $[\mu=1/(m_e^{-1}+m_h^{-1})]$ and ε is the dielectric constant. While the static value of the dielectric constant ε is often used in traditional semiconductors, the proper value of this quantity for 2D materials is often debated because of the large exciton binding energy. It has been suggested that the contribution of optical phonons to dielectric screening should be taken into account [27], and further investigations are necessary [28].

Deviation from this simple model has been explicitly observed in WS, monolayers [29]. Nevertheless, it provides a simple estimate of the exceptionally large exciton binding energy in TMD monolayers, which has been determined to be a few hundred milli-electron volts [29–32], or nearly two orders of magnitude larger than in conventional semiconductor quantum wells [33, 34]. This large binding energy originates from an increased effective mass [11] and the insufficient screening in the direction perpendicular to the 2D plane (Figure 2) and, consequently, an enhanced Coulomb attraction between electrons and holes and a small Bohr radius [14, 29, 32, 35–38]. The large binding energy of excitons, trions (an exciton bound with an extra electron or hole [12]), and higher order bound states such as biexcitons [39, 40] make these many-body states relevant for various optoelectronic devices, even at room temperature [41-44].

A small exciton Bohr radius leads to a large spatial overlap between the electron and hole wavefunctions and, therefore, a large oscillator strength as manifested in the strong exciton absorption (i.e. 5–10% for TMD monolayers). A large oscillator strength should, in

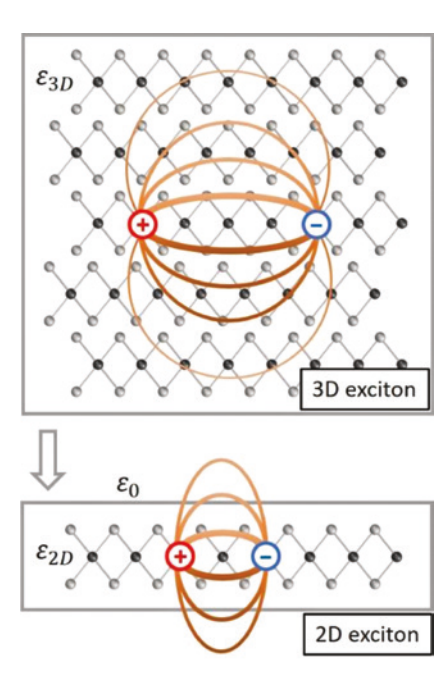


Figure 2: Illustration of Coulomb interaction leading to the formation of excitons, i.e. bound electron-hole pairs in a bulk and a 2D material.

principle, lead to a rapid radiative decay. Calculations suggest that the exciton radiative decay is on the order of a few hundred femtoseconds in perfect TMD monolayers [45, 46]. Deviations from ideal crystals lead to exciton localization and likely a longer exciton radiative lifetime. Directly measuring this radiative lifetime is difficult because commonly available techniques, such as pump/probe and time-resolved photoluminescence (PL), can only measure the total lifetime, determined by both radiative and nonradiative processes (we will discuss further this problem in Section 2.4). In addition, these experiments cannot distinguish intrinsic exciton recombination processes from those that repopulate the exciton resonances. Measurements often report a temperatureand excitation intensity-dependent exciton decay time, related to exciton-phonon and exciton-exciton interactions [46–50]. Ultrafast spectroscopy measurements have suggested that the total exciton recombination lifetime at low temperature is ~1 ps or shorter [51, 52]. This total lifetime is limited by the nonradiative decay because of the low quantum yield of commonly available TMD monolayers. Earlier measurements reporting longer lifetimes [46, 50, 53] were often limited by the temporal resolution of the technique. Exciton thermalization process following an impulse excitation further complicates the interpretation of the measured exciton decay times [54]. Placing TMD monolayers near plasmonic nanostructures likely shortens the lifetime further, making it even more difficult to accurately measure it. Explicit measurements of these dynamics in hybrid TMD-plasmonic materials are largely missing in the existing literature, despite being critical for enhanced light emission and modified valleytronic phenomena. The large oscillator strength also facilitates strong coupling to light, as reported in various coupled TMD-plasmonic systems [55, 56].

2.2 Single-photon emitters in TMD monolavers

Localized excitons, with completely different properties than 2D excitons, are also found in TMD monolayers. Indeed, several groups have reported that defects hosted in TMD monolayers (especially WSe₂) can trap excitons, and their subsequent radiative recombination features good single-photon emission properties at low temperature [18-20, 57, 58]. These excitons are typically localized at the flake edges and give rise to sharp emission lines (line widths \sim 100 µeV) that are red-shifted by 40–100 meV from the delocalized valley excitons [19] (Figure 3A). The quantum statistical properties of these single-photon emitters have been characterized by second-order photon correlation measurements [18–20, 57], and the measured lifetimes range from hundreds of picoseconds to few nanoseconds, similar to the values typically found in InAs self-assembled semiconductor quantum dots [60]. This long lifetime is in strong contrast with the short lifetime (~1 ps) of unbound excitons in ML TMDs, which is typically dominated by nonradiative decays.

High-resolution magneto-optical measurements have shown that the emission from these localized excitons is composed of a doublet (Figure 3B), which features orthogonal linear polarizations [18-20, 57]. When a magnetic field is applied perpendicular to the monolayer plane, the doublet splitting increases (Figure 3C) and the emission polarization evolves from linear to circular [19]; the handedness of circular polarization can be controlled by the magnetic field sign [19]. No clear dependence of the splitting and polarization on the magnetic field is observed when the field is parallel to the plane, similar to the case of unbound excitons.

The nature of these defects is not fully understood yet. It has been suggested that they can be due to vacancies, impurity atoms, or local strain [58]. Indeed, the defects initially investigated appeared mainly close to the edge of the monolayer, which limits their potential in practical applications. Many groups have therefore investigated the possibility of deliberately creating these defects with controlled positions. It has been shown that by placing ML

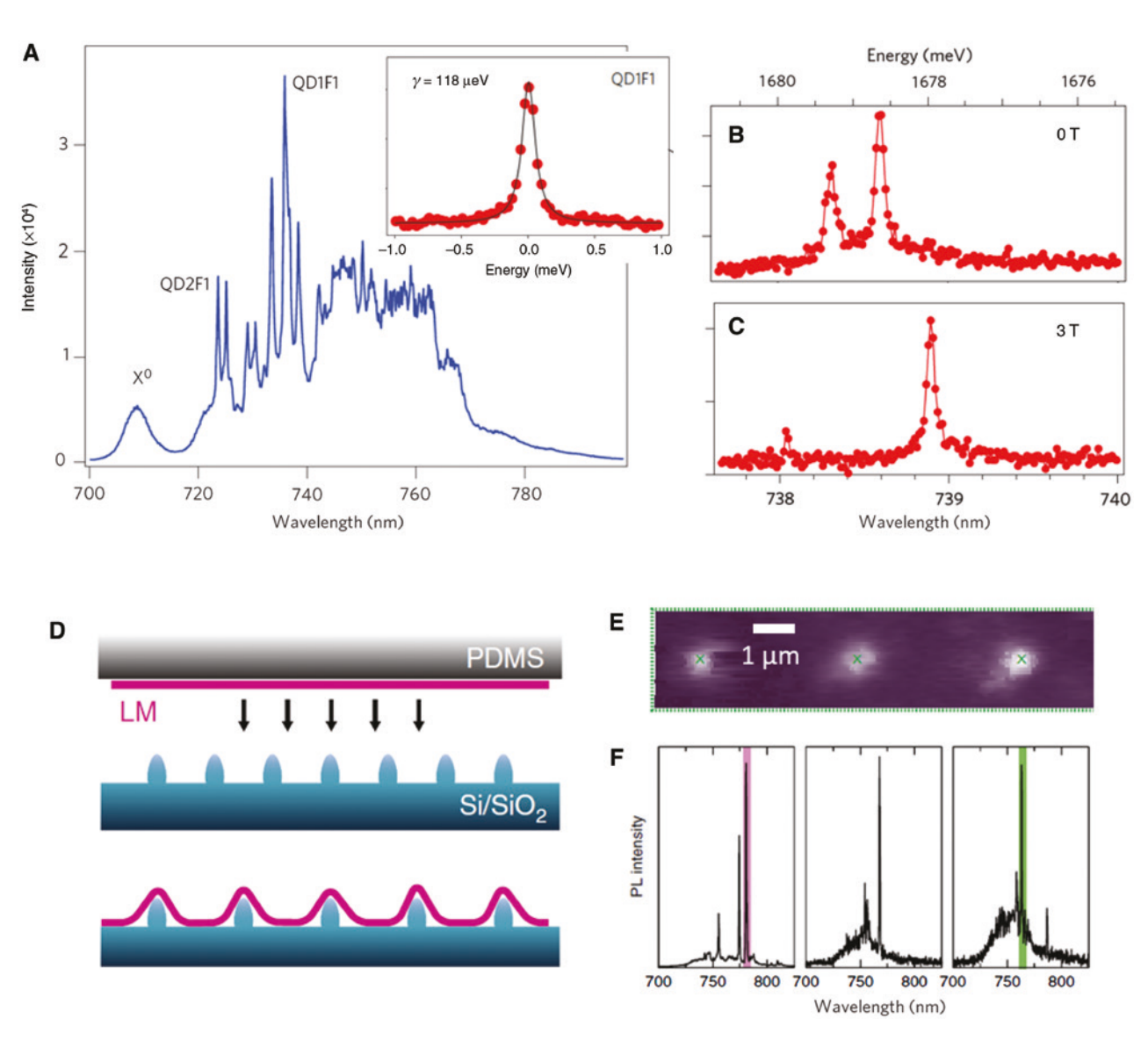


Figure 3: Single-photon emitters in monolayer TMDs.

(A) Low-temperature photoluminescence spectra of a monolayer WSe₂ flake, showing narrow emission peaks at energies lower than the excitonic emission X°. The inset shows a high-resolution spectrum for the peak labeled QD1F1. (B, C) High-resolution spectra of a different emission peak, showing the doublet structure in the absence of a magnetic field (panel B) and with a 3 T magnetic field (panel C) applied perpendicular to the monolayer plane. (D) A mechanically exfoliated TMD monolayer is deposited on an array of Si micropillar, introducing a local strained array. (E) Integrated PL intensity map of a region enclosing three nanopillars, indicated by the green crosses. (F) PL spectra taken at the three green crosses in panel (E). Panels (A–C) and (D–F) are adapted with permission from Ref. [18], Nature Publishing Group, and Ref. [59], Nature Publishing Group, respectively.

TMDs on dielectric [59] or metallic [61, 62] nanopatterned substrates, it is possible to induce a local strain pattern in the monolayer, which results in an array of quantum emitters. Palacios-Berraquero et al. [59], for example, deposited a WSe₂ monolayer on an array of silicon micropillars (Figure 3D). The PL intensity was highly enhanced at the position of the pillars (Figure 3E), and the PL spectra showed sharp single-photon emission lines (Figure 3F) with characteristics similar to those of emission centers randomly located at the flake edges.

2.3 Valley index in TMD monolayers

Valley refers to the energy minima or maxima in the electronic band structures, typically corresponding to the high-symmetry points in the reciprocal space of crystal [63–68]. While these valleys play an important role in electronic transport processes and optical transitions, the valley signature does not directly couple to external stimulants (e.g. electric or magnetic fields) in a specific way. Thus, it is usually not possible to manipulate the

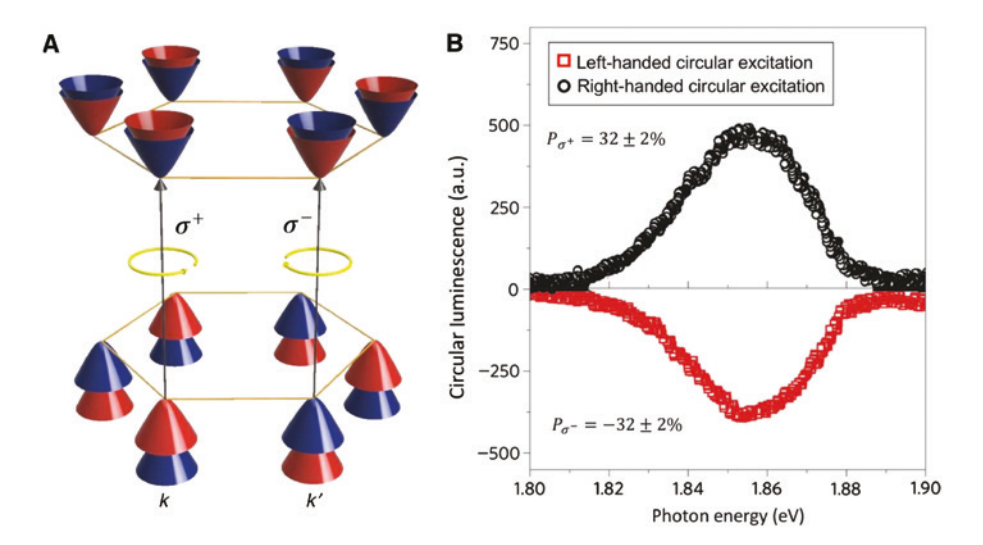


Figure 4: Valley-dependent optical selection rules in TMD monolayers. (A) Schematic of electronic band structure of TMD monolayer near the K and K' points in the Brillouin zone. The colors of the bands represent spin orientations (red: spin down, blue: spin up), which determine the optical selection rules. The optical transitions at the K and K' valleys are excited by the right-handed (σ) and left-handed (σ) circularly polarized light, respectively. (B) Circularly polarized PL spectra of MoS₂ monolayer under σ^+ (black circle) and σ^- (red square) optical pumping at 1.96 eV and T=10 K. Panel (B) is adapted with permission from Ref. [22], Nature Publishing Group.

degree of freedom of the valley. In monolayer TMDs, the valley-contrasting optical selection rules allow creating electrons, holes, or excitons with a particular valley index using circularly polarized light [4]. Indeed, excitons are formed at the corner of the Brillouin zone at two inequivalent valleys (Figure 4A), which are related to each other via time-reversal symmetry [21-23]. This binary degree of freedom has been proposed as an alternative way to represent information [4, 63, 64], similar to charges and spins. Upon optical excitation with circular polarization (e.g. σ), excitons or trions are created in one particular valley (e.g. the K valley). The degree of valley polarization can be quantitatively evaluated by $\rho = \frac{I(\sigma_+) - I(\sigma_-)}{I(\sigma_+) + I(\sigma_-)}$, where $I(\sigma_{\cdot})$ refers to the exciton PL intensity with σ_{\cdot} polarization. Interestingly, a recent theoretical work suggested that an asymmetry in the populations of the two valleys can be achieved even without a circularly polarized excitation beam, by shaping the vacuum field at the TMD location

Earlier experiments had reported that the subsequent PL maintains the chirality of the excitation source if the proper excitation laser wavelength is chosen [21-23, 70], inferring that the exciton valley index can act as a robust degree of freedom to carry information (Figure 4B). However, it is important to distinguish valley polarization associated with free carriers and the one with optical transitions such as excitons or trions [15, 16, 71–75]. The valley polarization of free carriers is long-lived because

with the aid of a polarization-dependent metasurface [69].

of the large energy splitting between states with opposite spins due to strong spin-orbit coupling in TMDs. Optical manipulation of valley index often relies on resonant excitations of excitons or trions. The valley polarization and coherence associated with excitons are quickly lost (~1 ps) as a result of the strong electron-hole exchange interaction [74, 76, 77]. In order to observe circularly polarized PL, the exciton valley polarization needs to be comparable to the exciton recombination lifetime, which is found to be typically ~1 ps (at low temperature) or shorter in TMD monolayers [51, 78]. This short lifetime is consistent with the large oscillator strengths or dipole moments associated with exciton transitions. Valley polarization associated with trions can be long under proper excitation conditions [74].

2.4 Control of the spontaneous emission with plasmonic structures

A quantum emitter generally radiates into all available photonic modes, and its radiative decay (i.e. decay accompanied by photon emission) competes with nonradiative channels. For an emitter placed in a bulk environment (indicated by the superscript 0), its total decay rate is given by the sum of the radiative (r) and nonradiative (*nr*) decay rates, $\gamma_{\text{tot}}^0 = \gamma_r^0 + \gamma_{nr}^0$. The intrinsic quantum efficiency (or quantum yield), $QE^0 \equiv \gamma_r^0 / \gamma_{tot}^0$, is often used to quantify the radiative efficiency of an emitter in a bulk environment. Excitons in TMD monolayers typically have an intrinsic quantum efficiency QE⁰ of 0.1–10% [42].

The bulk radiative decay rate γ_r^0 depends only on the emitter's dipole moment, frequency, and the material refractive index, and therefore it is normally difficult to manipulate. Moreover, in bulk materials photons are emitted into all available free-space radiation modes, making it challenging to harvest them. For many nanophotonic applications, and in particular toward the realization of single-photon sources for quantum information processing [79], it is necessary to achieve full control over the spontaneous emission: a quantum source must emit photons at a fast rate in order to overcome nonradiative decays and reduce the uncertainty of the emission time, and photons must be emitted into a single, well-defined mode with unitary efficiency [80–82].

Such control of the radiative process is possible because the radiative decay rate is not an intrinsic property of the emitter but depends on the local density of optical states (LDOS) available at the position and emission frequency of the emitter [83]. The LDOS, in turn, depends on the vacuum electric field created by the considered nanostructure. As a result, when an emitter is placed in a nonhomogeneous environment (such as an antenna or a cavity), its radiative decay rate is modified from γ_{r}^{0} to $\gamma_{r}(\mathbf{r}) = [F_{p}(\mathbf{r}) + 1]\gamma_{r}^{0}$, where we introduced the position-dependent Purcell factor $F_p(\mathbf{r})^1$. Importantly, as already mentioned above, time-resolved PL gives access to its total decay rate, rather than the radiative one. Thus, the total decay rate enhancement $\gamma_{tot}(\mathbf{r})/\gamma_{tot}^{0}$ [where $\gamma_{tot}(\mathbf{r})$ is the total decay rate of the emitter interacting with the nanostructure] is often used as a figure of merit in experimental works. Yet, it is important to keep in mind that the enhancement of the total decay rate is not always trivially related to an enhancement of the radiative decay rate (i.e. the Purcell factor). Indeed, the nonradiative decay rate γ_{nr}^{0} is normally not affected by a change in the electromagnetic environment. Moreover, when the emitter is placed close to a metallic surface, energy may be lost nonradiatively to the metal, which creates an additional nonradiative decay channel $\gamma_{\scriptscriptstyle M}$. It has been shown that $\gamma_{\scriptscriptstyle M}$ can become comparable to the radiative decay rate for dipolar emitters placed at few nanometers from a silver surface [86]. Therefore, the enhancement of the total decay rate can be expressed as

$$\frac{\gamma_{\text{tot}}(\mathbf{r})}{\gamma_{\text{tot}}^{0}} = \frac{[F_{P}(\mathbf{r}) + 1]\gamma_{r}^{0} + \gamma_{nr}^{0} + \gamma_{M}}{\gamma_{r}^{0} + \gamma_{nr}^{0}}.$$

Thus, only when the nonradiative and metal-induced decay rates are negligible can the Purcell factor be easily connected to the total decay rate enhancement. Moreover, when $\gamma_{\scriptscriptstyle M} \approx 0$, a measurement of the total decay rate enhancement gives always an underestimate of $F_p(\mathbf{r})$. A precise measurement of $F_p(\mathbf{r})$, therefore, requires the knowledge of the emitter's quantum efficiencies in the bulk and in the inhomogeneous environment.

In the simplest scenario where only one optical mode dominates the LDOS, the maximum achievable radiative enhancement is given by the well-known Purcell formula $\gamma_r/\gamma_r^0 = \frac{3}{4\pi^2} \lambda^3 Q/V$, where Q and V are the quality factor and the effective volume of the optical mode, respectively, and λ is the emission wavelength (in the medium) of the emitter. This maximum enhancement is obtained when the emitter is resonant with the cavity mode and it is positioned at the point of maximum field energy with the dipole moment parallel to the electric field. Large Q factors (i.e. small cavity loss) and small mode volumes are therefore crucial to enhance the radiative decay rate. The Purcell (i.e. radiative) enhancement has been intensively investigated in the last decades in both dielectric and metallic (or plasmonic) resonators. These two approaches offer complementary pathways to boost the ratio Q/V: dielectric resonators feature high Q factors but diffractionlimited mode volumes ($V \approx \lambda^3$), while plasmonic nanostructures provide sub-wavelength volumes ($V \ll \lambda^3$) but low *Q* factors due to the Ohmic losses. We note that subwavelength volumes can, in principle, be obtained also without metals, by exploiting very small dielectric discontinuities [87–90]. It is important to keep in mind that for open and/or plasmonic resonators, the derivation of the Purcell formula is ill-defined because of the complexvalued dielectric function and because the common definition of the mode volume leads to infinite values [91–93]. Interestingly, it has been demonstrated that the Purcell formula can still be used, provided that the definition of mode volume is properly generalized to take into account the leaky nature of the modes. Nevertheless, many experimental and theoretical works still use the standard expression of the Purcell formula (by taking the real part of a volume *V* calculated over a properly truncated region), as this is easier to compute, and it can provide an order-ofmagnitude estimate to guide the design of resonators and compare their performances.

Plasmonic modes are created by coherent oscillations of electrons in noble metals or heavily doped

¹ Note that in literature there are slightly different definitions of the Purcell factor. Here we follow the notation somehow prevalent in the TMDs community [84, 85] and define $F_p(\mathbf{r}) = (\gamma_r(\mathbf{r}) - \gamma_r^0)/\gamma_r^0$. In other cases, such as for solid state quantum dots [60], the definition $F_p(\mathbf{r}) = \gamma_r(\mathbf{r})/\gamma_r^0$ is instead often used. The formulas shown in this section can be easily modified for this alternative notation.

semiconductors, which couple strongly to the electromagnetic field and form polaritons. For extended surfaces, this results in waves termed surface plasmon polaritons (SPPs), which are tightly confined to the metal-dielectric interface and propagate along it. For metallic nanoparticles, the confined oscillation of the electrons gives rise to the localized surface plasmon resonances (LSPRs). The spectral response of LSPRs can be largely tailored by changing the particle shape and dimensions. Because of their capability of coupling a near-field source with farfield radiation (and vice versa), metallic nanoparticles are often termed plasmonic antennas in analogy with their radio wave counterpart [94-97]. The electric field of plasmonic modes is strongly confined near the nanoparticle surface, leading to large field enhancements and ultrasmall mode volumes, which are not diffraction-limited: volumes smaller than 10⁻³λ³ have been demonstrated in nanodisk resonators [98]. Therefore, despite their low Q factor due to the unavoidable Ohmic losses, plasmonic modes can still largely boost the ratio Q/V and lead to high Purcell enhancements while at the same time maintaining large radiative decay rates; in a recent experiment with silver nanocubes [99], total decay rate enhancements larger than 1000 were obtained, together with comparable or even higher enhancements of the radiative decay rate. Moreover, a low Q increases the operational bandwidth, which leads to two key advantages. First, it facilitates the spectral alignment between the emitter and the plasmonic mode, removing the need for post-fabrication tuning (which is often necessary for high-Q dielectric resonators). Second, due to the spectrally broad plasmonic resonance, a simultaneous enhancement of the nonresonant excitation field in PL experiments is also possible, further boosting the collected PL intensity.

While beneficial for the radiative decay rate enhancement, the ultra-small mode volumes of plasmonic resonators introduce a practical challenge for enhanced light-matter interactions. Since the electric field decays exponentially away from the particle surface (with a typical decay length of few tens of nanometers at optical frequencies), an emitter needs to be very close to the metal and optimally aligned to couple efficiently. This requirement has so far strongly limited the coupling of plasmonic structures with solid-state semiconductor emitters, such as quantum dots (QDs). Indeed, these emitters are usually embedded in a hosting 3D matrix, which therefore sets a minimum distance between the emitter and the metallic surface. Semiconductor quantum dots (SCQDs) in III-V materials, for example, need to be buried at least 30 nm below the surface to avoid a large increase of the nonradiative recombination rates [100]. This problem can be partially solved by passivating the surface [101], but the unavoidable embedding matrix still leads to limited [102-104] or absent [105] Purcell enhancements.

These challenges are absent when monolayers of TMDs are used as an active material: here, excitons are naturally embedded in a 2D sheet, and they can therefore be placed within few nanometers from a metallic surface. Recent experimental works have demonstrated PL enhancement larger than 10× with different geometries [106-108] and increase of the radiative decay rate larger than 300× in optimized resonators [84, 85, 109]. Moreover, the reduced dimensionality of the hosting matrix offers greater flexibility in terms of positioning and orienting the emitters with respect to the optical field, which can be exploited to reach an optimal alignment between the dipole moment and the plasmonic field [110].

3 Coupling emitters in TMD monolayers to plasmonic nanostructures and metasurfaces

In this section, we discuss different implementations that have been proposed and demonstrated in recent years to couple TMD monolayers to plasmonic antennas and devices. We will focus in particular on works where plasmonic-induced enhancement of photoluminescence and decay rate have been shown. In Table 1, we summarize the results of the studies reviewed in this section.

3.1 Coupling of mobile excitons to plasmonic antennas

A well-investigated approach to couple ML TMDs to plasmonic antennas consists in fabricating the metallic structures directly on top of the TMD layer with conventional lithographic techniques. Several groups have used this method to study plasmonic-induced PL enhancement of mobile excitons in TMD monolayers [106, 107, 111]. Butun et al. [107] placed square arrays of silver nanodisks on top of a MoS₂ monolayer (Figure 5A) and measured the roomtemperature PL from the A exciton in MoS, in the spectral range 650-750 nm. PL enhancements larger than 10× were found for some nanodisk diameters (Figure 5C). Moreover, the maximum enhancement occurs at a particular emission wavelength, which red-shifts as the nanodisk diameter increases (Figure 5B); thus, while a contribution from excitation enhancement cannot be ruled out, the observed PL enhancement is necessarily related to an increased

Table 1: Summary of the performance of several plasmonic/TMD systems discussed in the text.

Plasmonic structure/TMD material	Temperature	Spectral feature investigated	Peak PL enhancement	Modified lifetime	Decay rate/Purcell enhancement	Reference
Plasmonic structures fabri	cated on top of	TMD monolayers				
Ag nanodisks/MoS ₂	RT	ME	12×	_	_	[107]
Ag bowties/MoS ₂	RT	ME	$16 \times (A)$, $25 \times (B)$. EE = $1.8 \times$	_	_	[106]
Au bowties and dimers/	RT	ME	8× (bowties) 6× (dimers)	_	-	[111]
Ag slot antenna/WSe ₂	RT	ME	700×, EE = $2.2 \times a$	-	~300a	[109]
TMD monolayers draped or	ver plasmonic s	structures				
Ag nanotriangles and islands/WSe ₂	LT (10 K)	ME (~705 nm) and LE (>720 nm)	20× (LE/nanotriangles) 8× (LE/islands) Quenching of ME	-	-	[108]
Si-Au-Al ₂ O ₃ nanopillars/ WSe ₂	LT (3 K)	Induced LE (>720 nm)	2×	2.2 ns ^b	2.4 ^b	[84]
Ag MIM waveguide WSe ₂	LT (3 K)	Induced LE (>720 nm)	-	3.34 ns ^c	1.8 ^c	[110]
Au nanocubes/WSe ₂ /Au mirror	LT (4 K)	Induced LE (750–800 nm)	-	$266\pm120~ps^d$	181 ^d	[85]

We only included works where enhancements of photoluminescence (PL) or decay rate were reported. In the column "Decay rate/Purcell enhancement", the accompanying footnote specifies for each case which of the two enhancements is reported and how it is calculated. When available, we have indicated the fraction of the PL enhancement due to the enhancement of the excitation (EE).

efficiency of the emission into the plasmonic resonance of the single nanodisk. Similar values of PL enhancements were also reported by Lee et al. [106] in samples made of a square array of silver bowtie antennas placed on a MoS₂ monolayer (Figure 5D, E). Palacios et al. [111] fabricated 40-nm-thick gold dipole and bowtie antennas on top of a MoS₂ monolayer. The maximum PL enhancement depended sensitively on the in-plane dimensions and was found to vary from 1.4 to 4.5 for the dipole antennas and from 4.1 to 8.40 for the bowtie antennas. No marked correlation between the antenna dimensions and the wavelength at which the maximum PL enhancement occurs was found, indicating that, in this experiment, the plasmonic structures mainly provided a nonresonant excitation enhancement.

A different approach, which ensures self-alignment between a nanostrip monolayer of WSe₂ and a slot antenna, was recently proposed by Eggleston et al. [109] (Figure 5F–I): the TMD monolayer was deposited on a sacrificial substrate and covered by SiO_x; a lithographically defined mask was then used to etch away the TMD/SiO_x

everywhere except on small rectangular strips. Without removing the mask, a thick layer of silver was evaporated on the sample, thus realizing a metallic slot cavity automatically aligned with the TMD strip (Figure 5F). Because of the high electric field enhancement at the TMD position (Figure 5G), and because of the fact that any portion of the TMD layer outside the antenna was removed, a very large PL enhancement was obtained, up to ~700× (Figure 5H, I). The PL enhancement was maximized when the plasmonic resonance supported by the nanoslot was tuned to the peak wavelength of the exciton emission (Figure 5H, I, A1 curve). The total enhancement was due to a combination of increased excitation, improved collection efficiency, and higher radiative decay rate. The authors estimated numerically that the antenna was able to redirect 48% of the radiation into the objective numerical aperture, compared to a value of 17% for a bare sample. This effect, combined with a small pump enhancement (and the fact that only the dipole moments in the material parallel to the slit contribute to the enhancement), led to an overall enhancement of

RT, room temperature; LT, low temperature; ME, mobile exciton; LE, localized exciton.

^aThe excitation enhancement (EE) includes also the enhanced collection efficiency. The decay rate enhancement was not obtained through time-resolved measurements, but estimated from the PL enhancement and the numerically calculated antenna efficiency and quantum yield. b"Modified lifetime" is the average over 48 different emitters interacting with plasmonic nanopillars. The decay rate enhancement is calculated by dividing the modified lifetime by the average lifetime of 39 emitters in a bare flake.

c"Modified lifetime" is the average over seven different emitters located on the waveguide. The decay rate enhancement is calculated by dividing the modified lifetime by the average of the lifetime of 10 emitters in a bare flake.

^dThe quoted values are averaged over 12 emitters. Purcell enhancement is calculated separately for each emitter, by correcting the reduced lifetime with the enhanced quantum yield. The highest Purcell factor obtained was 551.

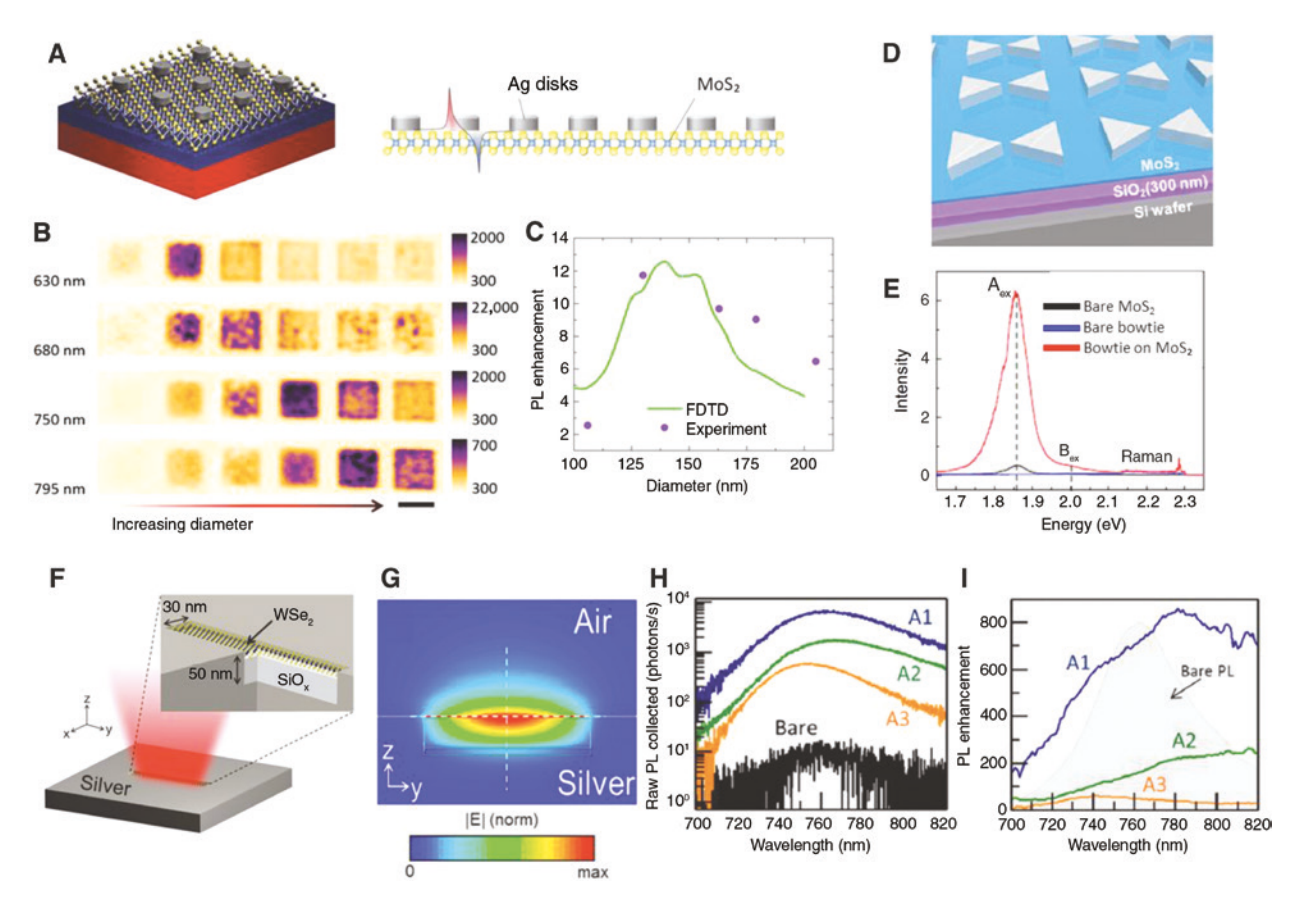


Figure 5: Coupling excitons in monolayer TMDs to plasmonic antennas.

(A-C) An array of silver nanodisks placed on top of a MoS, monolayer, (B) PL emission 2D spatial maps at four different wavelengths (rows) and six different nanodisk diameters. Diameters of the disks are 106, 130, 163, 179, 205, and 227 nm from left to right. (C) Comparison between calculated composite electric field enhancement and measured PL enhancement. (D, E) An array of silver bowties placed on top of a MoS, monolayer. (E) PL emission from the bare MoS,, the bare bowtie array, and the composite system. (F-I) A silver slot antenna aligned with a nanostrip of WSe,. (G) Calculated electric field enhancement provided by the slot antenna. (H-I) PL intensity from a bare WSe, layer and from three different antenna-TMD systems with different antenna dimensions. (I) PL enhancement obtained from panel (H); the shaded gray curve shows the PL spectrum of the bare monolayer. Panels (A-C), (D, E), and (F-I) are adapted with permission from Ref. [107], American Chemical Society; Ref. [106], American Chemical Society; and Ref. [109], American Chemical Society; respectively.

the collection efficiency by 2.2x. The radiative emission enhancement was therefore estimated to be 318×.

3.2 Coupling of defect-bound excitons to plasmonic structures

A different approach to realize coupled TMD-plasmonic systems consists in draping a TMD monolayer over a nanopatterned substrate. Several works have used this method with dielectric [59] or metallic structures [61, 62, 84, 85], and it has been suggested that the strain induced in the TMD layer by the substrate creates local potential minima, leading to localization centers for excitons.

Johnson and coauthors [108] investigated a sample composed of WSe, flakes transferred on to either a silver

nanotriangle array, a uniform silver island, or a bare SiO substrate (Figure 6A, B) and measured the low-temperature PL in the three different cases. The single triangles support a broadband, localized plasmonic resonance centered at 645 nm, which partially overlaps with the emission from the mobile (~715 nm) and the localized (>720 nm) excitons in WSe₃. The authors found that the emission from the localized excitons was enhanced by the metal environment: the low-temperature (10 K) PL enhancement (spectrally integrated in the range 720-80 nm and calculated with respect to the case of a bare SiO₂ substrate) was found to be ~8× for the Ag island and $\sim 20 \times$ for the nanotriangle array. When considering the actual area occupied by the nanotriangles, the normalized enhancement factors increased to ~200×. This large enhancement was likely due to a combination of decay rate enhancement and increased light absorption,

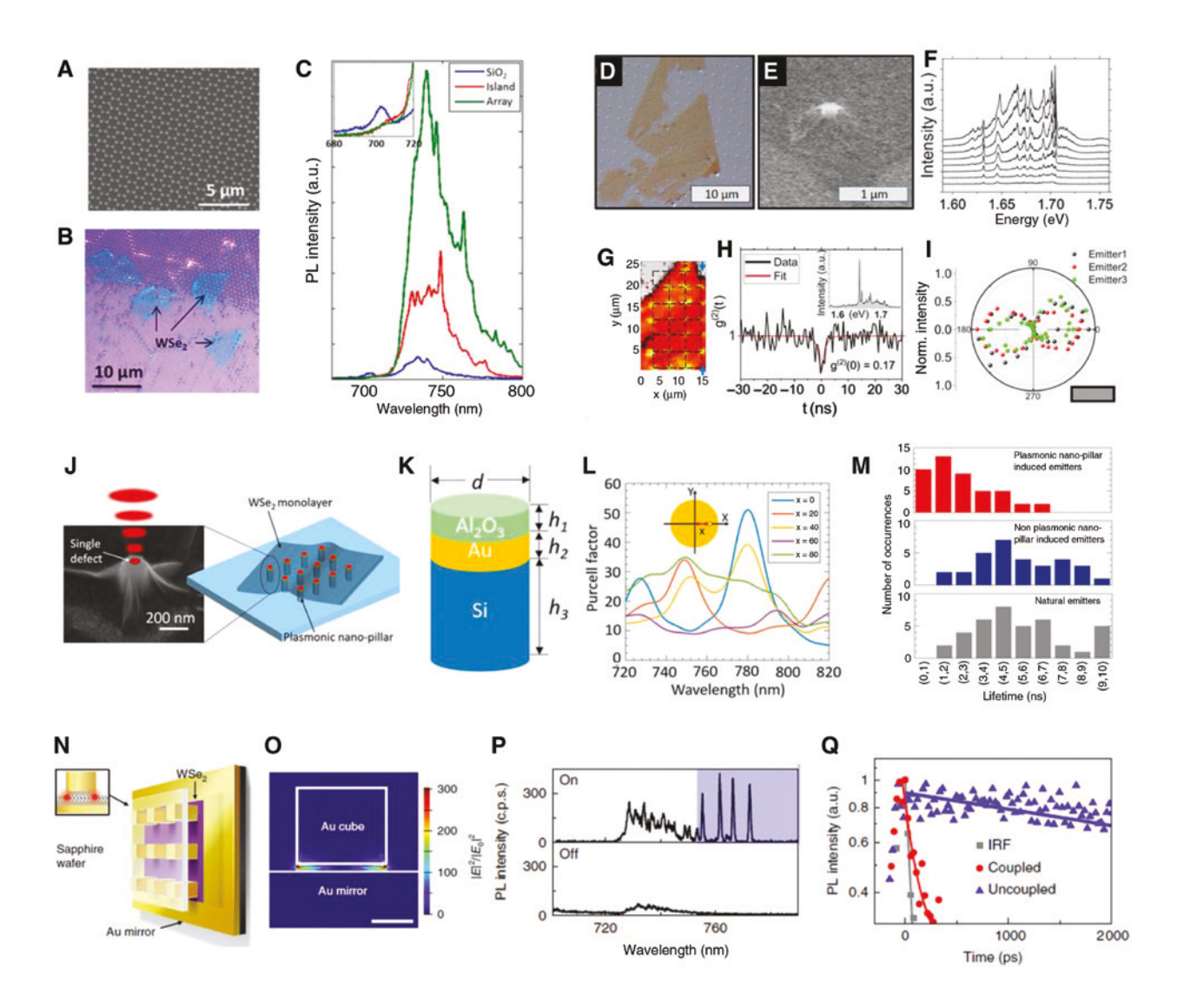


Figure 6: Coupling defect-bound excitons to plasmonic antennas.

(A–C) A WSe₂ monolayer draped on an array of silver nanotriangles. (A) SEM image of the plasmonic array. (B) Optical image of the WSe₂ flakes placed on the antenna array. (C) PL intensity when the WSe₂ flakes are placed on the array (green curve), on a flat silver island (red curve), or a SiO₂ substrate. (D–I) A WSe₂ monolayer draped on an array of gold nanopillars. (D, E) SEM images of the nanopillar array with the WSe₂ flake on top, and a zoom-in view of a single nanopillar. (F) Power-dependent PL spectra from a single nanopillar. (G) Spatial PL map of WSe₂ flake covering the nanopillar array. (H) Second-order autocorrelation function of a single quantum emitter on a pillar. (I) Polarization characteristic of three individual emitters placed on different horizontally-aligned pillars. (J–M) A WSe₂ monolayer draped on an array of plasmonic nanopillars. (J) Schematic of the sample geometry. (K) Layout of a single nanopillar. (L) Calculated Purcell factors of an emitter versus its wavelength and its distance (x) from the nanopillar center. (M) Statistical comparison of lifetimes of single-defect emitters in bare WSe₂ monolayers (bottom) and for emitters induced by plasmonic (top) and nonplasmonic (middle) nanopillars. (N–Q) Large Purcell enhancement obtained with gold nanocubes. (N) Schematic of the sample, with a WSe₂ layer sandwiched between a gold mirror and an array of nanocubes. (O) Near-field distribution of electric field intensity enhancement created by the nanocube. (P) PL spectra from a bare sample ("off") and from a WSe₂ monolayer strained over the Au nanocubes. (Q) Lifetime measurement of the same emitter from a WSe₂ monolayer placed on the nanocubes without ("uncoupled") and with ("coupled") the gold mirror. Panels (A–C), (D–I), (J–M), and (N–Q) are adapted with permission from Ref. [108], American Chemical Society; Ref. [61], The Optical Society; Ref. [84], American Chemical Society; and Ref. [85], Nature Publishing Group; respectively.

but the lack of lifetime measurements prevented the quantitative evaluation of the two contributions separately. Remarkably, the authors observed that the emission from the mobile excitons was, instead, quenched when the WSe.

ML was on the plasmonic structures (either on the Ag film or Ag nanotriangle array). This observation is consistent with the different relaxation dynamics for the mobile and localized excitons. The PL spatial maps acquired in this work showed that the defect-bound emitters were mainly localized at the flake edges and that the strain induced by draping the WSe, layer on the nanotriangles did not create additional defects.

A similar approach has been used by different groups to demonstrate that the strain induced by a nanopatterned array could be used to obtain ordered arrays of quantum emitters. Iff et al. [61] utilized square arrays of gold nanopillars on a SiO, layer with conventional lithography techniques. The array pitch was large enough (4 µm) so that each pillar could be addressed individually in optical experiments. An atomically thin layer of WSe, was then transferred onto the pillar array (Figure 6D). For most of the nanopillars, this resulted in a locally strained layer, leading to a tent-like structure (Figure 6E). A spatially resolved PL study showed a high correlation between bright emission spots and the position of the metallic pillars (Figure 6G). The low-temperature emission spectrum featured several sharp peaks below the free exciton energy (<1.74 eV) (Figure 6F), which the authors associated with strongly localized excitons due to strain. Second-order autocorrelation measurements (Figure 6H) showed $g^{(2)}(0) = 0.17$ and confirmed the single-photon emission from these peaks. Moreover, for asymmetric pillars, a strong correlation between the polarization of light and the long axis of the pillar was found (see Figures 6I and 3D in Ref. [61]), indicating that the exciton emission was strongly modified by the localized plasmonic mode. Cai and coauthors utilized a similar system composed of hybrid dielectric-metallic nanopillars (Figure 6J, K) to demonstrate enhancement of the decay rate of the localized excitons [84]. The low-temperature PL spectra from each nanopillar showed one or multiple narrow peaks, indicating the formation of localized emission centers, whose single-photon nature was confirmed by $g^{(2)}(0)$ measurements. The nanopillar design was optimized to induce a large Purcell factor (>50) for an emitter positioned on top of it and emitting at 780 nm (Figure 6L). The authors measured the lifetime of 46 single-defect emitters located on the plasmonic nanopillars (Figure 6M, top). They then compared these to a similar number of emitters in two control groups, one with dielectric nanopillars without gold (Figure 6M, middle) and the other in the bare material with no nanopillars (Figure 6M, bottom). The average lifetime of the emitters in the bare material $(T=5.3\pm2.3 \text{ ns})$ was not statistically changed for the emitters interacting with non-plasmonic nanopillars ($T=5.2\pm2.1$ ns). The average lifetime of the emitters interacting with the plasmonic nanopillars was, instead, reduced to $T=2.2\pm1.5$ ns, indicating an enhancement of the total decay rate of 2.4.

In most studies discussed so far (and in the next section), the PL and decay rate enhancements have been

calculated by averaging the lifetimes of ensembles of emitters coupled and uncoupled with a plasmonic structure, and modest values of decay rate enhancements have been demonstrated. In a recent experiment, Luo and coauthors have demonstrated a method (inspired by Ref. [99]) to achieve large radiative enhancements and, at the same time, to measure the bare and enhanced decay rates of the same emitter [85]. A WSe, was transferred onto an array of gold nanocubes fabricated on a sapphire substrate, and a gold flat layer was then attached on the other side (Figure 6N). The vertical plasmonic gap mode obtained featured a very large field enhancement near the nanocube edges (Figure 60). The low-temperature PL spectra acquired from each nanocube showed a set of sharp peaks in the 755-790 nm spectral region (Figure 6P). In most cases, exactly four spectrally isolated emitters were found per site, leading the authors to suggest that each corner of a nanocube was coupled to one quantum emitter. The lifetime of each emitter was measured before and after placing the flat gold layer, thus allowing the lifetime variation of each emitter to be evaluated. The authors found that the lifetime could be reduced by a factor as high as 57 (Figure 6Q), which led to a Purcell factor of 551 after correcting for the variation of the quantum efficiency.

3.3 On-chip guiding of single photons extracted from TMD materials

As discussed in the previous section, several works have demonstrated the coupling of light emitted by either localized or mobile excitons in ML TMDs to plasmonic nanocavities or arrays. However, the light collected by these structures is then re-emitted directly into the far field, thus hindering any application for plasmonic circuitry and, in general, for on-chip manipulation of the optical signal. The possibility of coupling defectbound excitons to propagating surface plasmons has been demonstrated in a few recent works. In the work of Cai et al. [112], a sheet of atomically thin WSe, was transferred onto the top of a chemically synthesized silver nanowire (Figure 7A). The strain induced by the nanowire created localized and optically active defects in the WSe, layer, as demonstrated by a spatial map of the PL intensity (Figure 7B). The low-temperature emission spectrum (Figure 7C) featured several sharp lines, each consisting of a doublet corresponding to the two different in-plane polarizations of the localized exciton. The single-photon nature of the emission was proven by a second-order correlation measurement of the emission

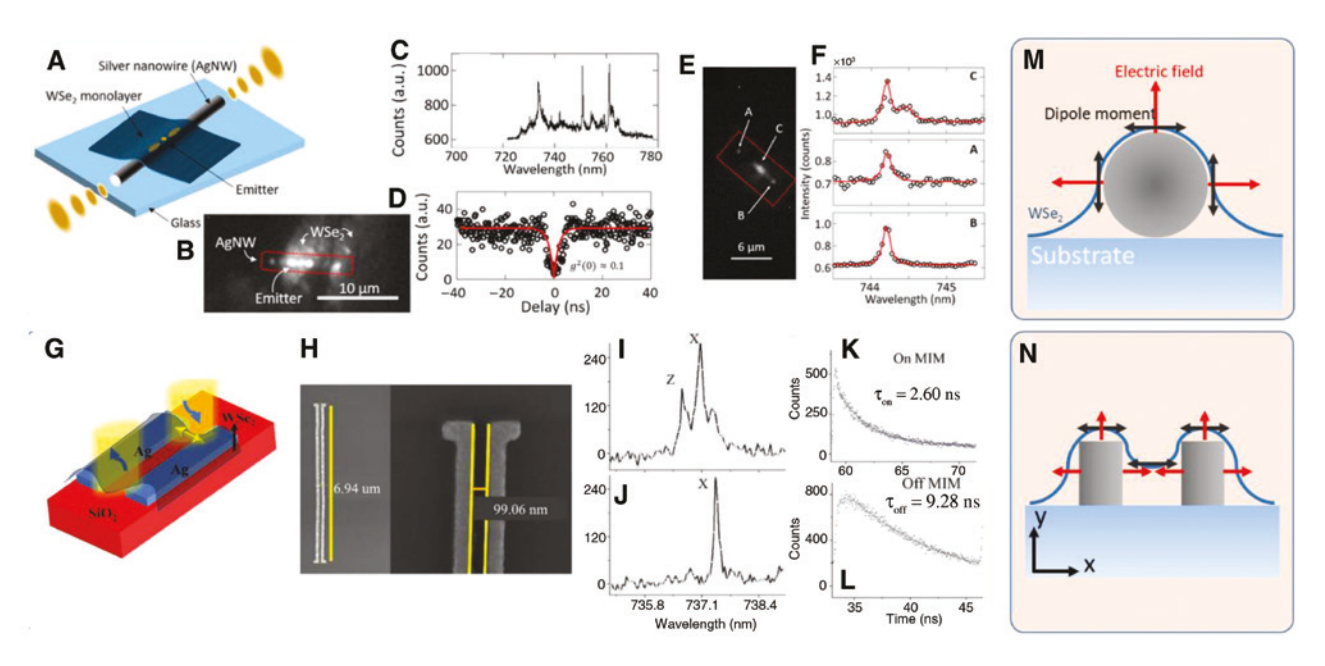


Figure 7: On-chip coupling between excitons and propagating SPPs along plasmonic waveguides. (A–F) A WSe₂ monolayer coupled to a silver nanowire. (B) PL spatial map of the TMD–nanowire system. (C) Emission spectrum from one of the localized spot in panel (B). (D) Second-order autocorrelation function of one of the peaks in panel (C). (E) Spatial map of PL when exciting at the center of the nanowire (point C). (F) High-resolution PL acquired from points C, A, and B in panel (E), when exciting at point C. (G–L) A WSe₂ monolayer coupled to a silver metal-insulator-metal waveguide. (H) SEM pictures of the waveguide. (I) PL spectrum when exciting the structure on one edge of the waveguide and collecting from the same point. (J) As in panel (I), but collecting from the opposite edge of the waveguide. (K–L) Lifetime of a representative emitter located close to the waveguide (panel K) and of a different emitter located far away from the waveguide (panel L). (M, N) Schematic of the alignment between the plasmonic field and the exciton dipole moment in the two waveguide geometries. Panels (A–F) and (G–L) are adapted with permission from Ref. [112], American Chemical Society, and Ref. [110], AIP Publishing, respectively.

into free space (Figure 7D). Because of their proximity, these defects coupled efficiently to propagating surface plasmons sustained by the nanowire. Upon laser excitation at the nanowire center (point C in Figure 7E), emission was also observed from the nanowire ends (points A and B). Importantly, while the emission from the nanowire center showed the doublet structure mentioned above (Figure 7F, top panel), the emission from the nanowire ends showed only one peak (Figure 7F, center and bottom panels). The authors attributed this behavior to the fact that, due to their different polarizations, only one of the two quasi-degenerate localized excitons coupled efficiently to the nanowire and propagated from the center to the edges. By measuring the intensity of light emitted from the nanowire ends for 21 different nanowires, the authors estimated an average coupling efficiency of 26%±11%. In this approach, the coupling efficiency was affected by an unfavorable plasmon-exciton geometrical alignment (Figure 7M): the electric field vector of the nanowire plasmonic mode is mainly perpendicular to the metal surface and directed radially outward, while the excitons have inplane dipole moments, tangential to the metal surface.

Because of this poor alignment, no enhancement of the decay rate was observed in this study. In order to improve the coupling, the same group demonstrated a different design based on a metal-insulator-metal waveguide (Figure 7G-L) [110]. Two silver rectangular stripes, separated by a small air gap, were fabricated on top of a SiO, substrate, realizing a slot waveguide. The electric field of the resulting guided mode is strongly localized in the air gap and, importantly, its main component is in plane and orthogonal to the waveguide direction. Thus, when a WSe, monolayer was transferred onto the top of the structure, the dipole moment of a defect-bound exciton in the air gap region was quasi-optimally aligned to the electric field of the guided mode (Figure 7N). Similar to the case of the nanowire, the emission spectrum from the excitons was a doublet (Figure 7I), and only one of the two emission peaks was visible when collecting light from the opposite end of the waveguide (Figure 7J) as a result of the different in-plane polarizations. By measuring the lifetime of 10 emitters located on the pristine monolayer and 7 emitters located on the waveguide/ monolayer (see Figure 7K, L for representative measurements), the authors estimated a lifetime reduction of ~2.

4 Coupling valley index to plasmonic nanostructures and metasurfaces

4.1 Enhancing valley polarization with plasmonic nanostructures

Because of the low quantum efficiency of available TMD monolayers [10, 113], the PL intensity can be drastically enhanced by placing a monolayer near plasmonic antennas in various geometries, such as bowtie or gap plasmons, as was shown in the experiments reviewed in the previous sections. Enhancing exciton valley polarization, on the other hand, requires a more careful design of the

near field. There are a number of reasons why the presence of a plasmonic nanostructure or a metasurface can enhance valley polarization. In addition to shaping the polarization of the near field, the presence of a plasmonic structure may shorten the exciton recombination lifetime via the Purcell effect while having minimal influence on valley scattering time.

In a recent work, Ziwei and coworkers [114] investigated a sample composed of a ${\rm MoS_2monolayer}$ sandwiched between a chiral metasurface and a Au film (Figure 8A). The scanning electron microscopy (SEM) images of the metasurface and of the hybrid structure are shown in Figure 8B and C, respectively. In the absence of a metasurface, a finite valley polarization $\rho \sim 25\%$ was observed in PL for both σ^- and σ^+ excitation conditions with the excitation wavelength of 633 nm and at 87 K (Figure 8D, G

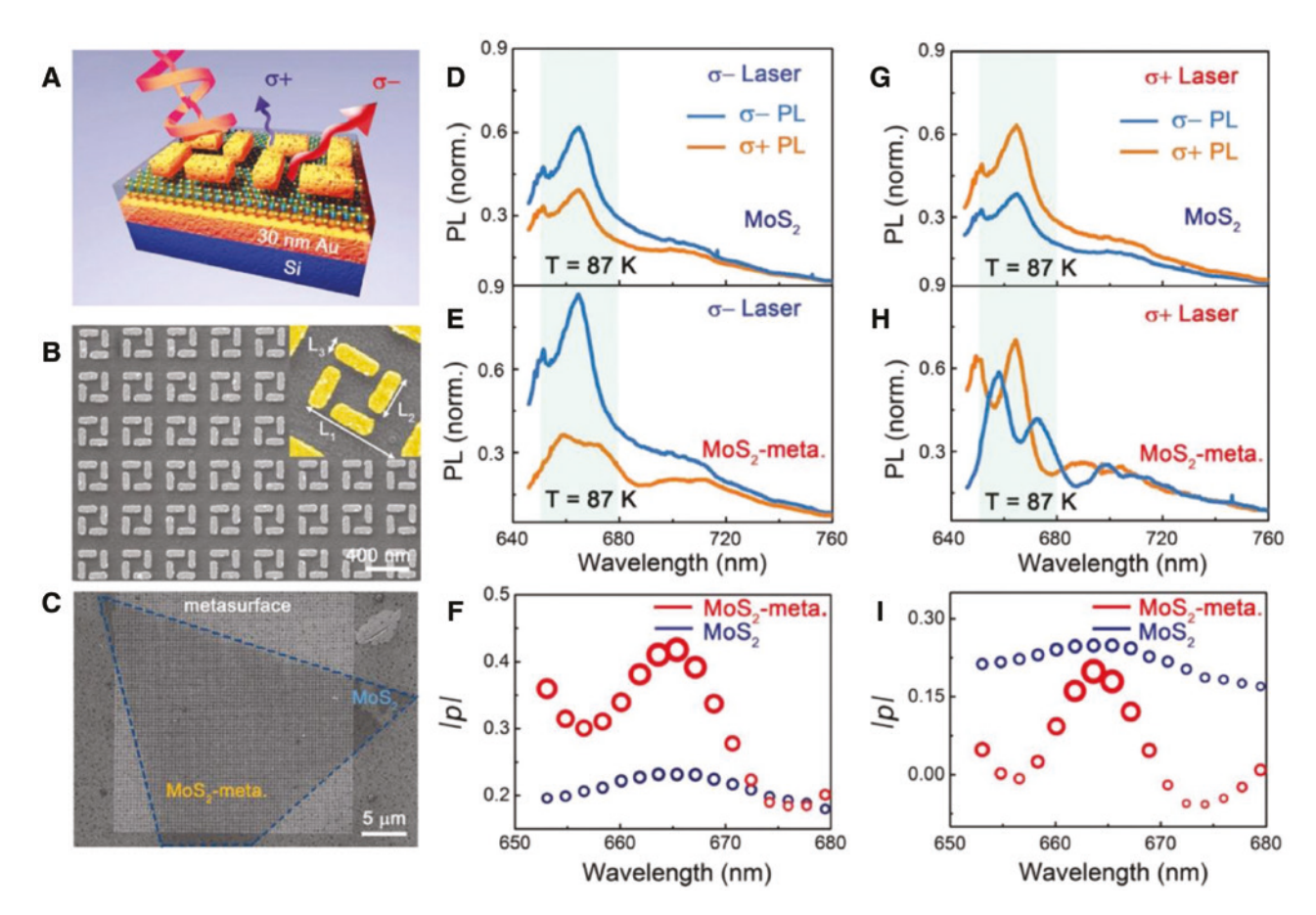


Figure 8: MoS_2 -metasurface hybrid system and its valley-polarized PL spectra. (A) Schematic of hybrid MoS_2 -metasurface structure, where the chemical vapor deposition (CVD)-grown MoS_2 monolayer is between a chiral metasurface layer and a 30-nm-thick Au film. (B) SEM image of the metasurface fabricated by e-beam lithography. Inset shows the SEM image of one unit. (C) The SEM image of MoS_2 -metasurface hybrid structure. The triangle shape of MoS_2 monolayer is shown as the blue dotted lines. (D, E) Circularly polarized PL spectra of the MoS_2 monolayer (D) and the hybrid MoS_2 -metasurface (E) under σ optical pumping (633 nm) at T= 87 K. (G, H) Same as in panels (D, E), but for under σ optical pumping. Degree of valley polarization (DVP) plots for MoS_2 monolayer and hybrid MoS_2 -metasurface are shown under (F) σ pumping and (I) σ pumping. An increase of DVP from 25% to 43% with σ pumping is observed, while a decrease of DVP from 25% to 20% with σ pumping is seen. Panels are adapted with permission from Ref. [114], John Wiley and Sons.

and blue circles in Figure 8F, I). For the hybrid TMD-plasmonic structure, at the A exciton energy around 665 nm, ρ increased to 43% with σ excitation (Figure 8E and blue circles in Figure 8F), while it decreased to 20% with σ^+ excitation (Figure 8H and blue circles in Figure 8I). This result can be explained by considering the exciton dynamics in the hybrid structure. For K' valley excitons, both the generation and emission rates of excitons are enhanced as a result of the interaction between the MoS, monolayer and the metasurface. In contrast, K valley exciton emission is suppressed. Meanwhile, the intervalley scattering rate mainly depends on the temperature and the excitation wavelength, thus largely unchanged in the presence of the metasurface. The enhanced or reduced exciton valley polarization results from the competition of exciton generation, emission, and the intervalley scattering rate.

4.2 Directing valley exciton emissions

Plasmonic antennas have been shown to significantly modify the emission rate, radiation pattern, and sometimes the polarization, as discussed above. Plasmonic devices can also be used to direct emission from valley polarization excitons toward different directions, effectively serving as a link between photonic and valleytronic devices [115]. A conceptually simple design has been proposed by Chen and coworkers [116] (Figure 9A). By coupling circularly polarized dipoles (i.e. valley excitons) to plasmonic antennas that support both dipole and quadrupole modes, the interference between the two plasmonic modes can be exploited to direct emissions from opposite valleys to different directions (Figure 9B). When the phase between dipole and quadrupole modes changes by π , the emission is directed to the opposite direction.

A metasurface designed to direct valley-selective emission from a monolayer WS, has been demonstrated by Chervy and coworkers [115] (Figure 10A). The metasurface consists of a series of rectangular nanoapertures in a gold film rotated stepwise along one axis by an angle $\phi = \pi/6$. These rotating apertures are further arranged in a square lattice with a grating period Λ , setting up a rotation vector of $\Omega = (\phi / \Lambda)\hat{z}$. The gradient of the geo-

metric phase adds a momentum term $k_g = -\sigma \left(\frac{\phi}{\Lambda}\right)\hat{x}$ to

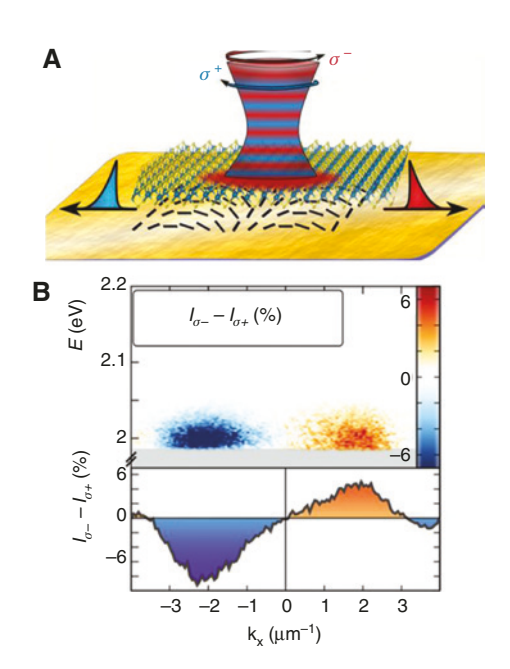


Figure 10: Directing emissions from valley excitons in a WS. monolayer with a chiral metasurface at room temperature. (A) Schematic of propagation of spin-momentum-locked SPPs with opposite chirality. (B) Momentum-resolved differential PL under σ^+ and σ optical pumping. Panels are adapted with permission from Ref. [115], American Chemical Society.

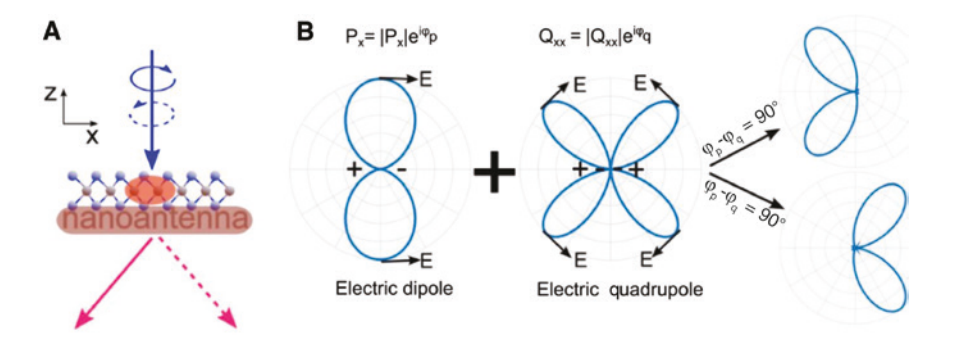


Figure 9: Directing valley-dependent emission using a nano-antenna. (A) Schematic of TMD layers coupled to a double-rod nano-antenna, which separates emission from opposite valleys. (B) The directional emission is due to the interference between the electric fields from an electric dipole and quadrupole. The direction is determined by the relative phase of the dipole and quadrupole. Panels are adapted with permission from Ref. [116], Beilstein-Institut zur Förderung der Chemischen Wissenschaften.

the phase-matching condition for the SPP excitation: $k_{\rm SP} = k_{\rm in} + (2\pi/\Lambda)(n\hat{x} + m\hat{y}) + k_{\rm g}$, where $\sigma = \pm 1$ is the photon helicity. The optical spin-orbit interaction locks the propagating SPP modes corresponding to $n=\pm 1$ with the photon helicity $\sigma=\pm 1$. Therefore, SPPs launched on a bare metasurface propagate in opposite directions if chirality of the excitation field is reversed, as illustrated in Figure 10A.

The strong coupling between excitons and SPPs, due to the exceptionally large exciton oscillator strength, leads to the formation of polariton states, as evidenced by the anti-crossing dispersion in the angle-resolved absorption spectra [117, 118]. The valley index is inherited by the exciton-SPPs. The PL from these chirality-dependent polariton states is separated in k-space resolved measurements, as shown in Figure 10B. Interestingly, the authors did not observe valley polarization from PL from a bare WS, in the excitation conditions adopted. The enhanced valley polarization and valley coherence associated with the exciton-SPPs suggest that these hybrid modes may be more suitable for optical manipulation of valley index than excitons hosted in bare TMD monolayers.

4.3 Spatial separation of valley index

Another prerequisite to build valleytronic devices is the capability of separating carriers and quasiparticles with different valley indexes. Several strategies based on various Hall effects have been explored [119-124]. For example, the valley Hall effect in monolayer TMDs has been proposed [64] and later experimentally demonstrated [124]. In this phenomenon, the valley-specific Berry curvature acts as a momentum-dependent synthetic magnetic bias, leading to transverse separation of valleypolarized free carrier driven by the in-plane electric field in the perpendicular direction. Very recently, the exciton valley Hall effect was demonstrated [125], where the valley-polarized excitons were separated in the presence of a laser-induced temperature and exciton density gradient. However, these previous valley separation schemes were demonstrated only at low temperature, thus limiting their use in practical applications.

4.3.1 Chiral photonics

In a different context, optical spin-orbit interaction enables the separation of optical spins and directional propagation of electromagnetic waves with chiral polarizations [126–129]. Such chirality-dependent propagation can be understood within a near-field interference picture [130]. Consider a circularly polarized dipole $(P_x + iP_x)$ placed in the vicinity of a waveguide surface, as illustrated in Figure 11A. This dipole excites the guided modes in the waveguide, with the horizontal component of the dipole (P_n) driving the longitudinal field and the vertical component (P_{α}) coupling to the transverse field of the guided electromagnetic mode. The magnetic field $H_{i}(k_{i})$ induced by $P_{\nu}(P_{\nu})$ is symmetric (antisymmetric) respective to k_{x} . Therefore, the linear superposition of the two orthogonal dipoles P_{x} and P_{z} leads to a nonsymmetric spatial frequency distribution. The guided modes with $k_{\downarrow} > 0$ ($k_{\downarrow} < 0$) interfere destructively (constructively). This near-field interference is the mechanism for the chiralitydependent, unidirectional excitation of guided modes. As an example, Figure 11B shows the calculated magnetic field distribution at a metal/dielectric interface induced by a circularly polarized dipole. While both counter-propagating SPP modes are supported on the metal/dielectric interface, only one of these modes is predominantly excited by the circular dipole, leading to chirality-dependent SPP propagation.

The optical spin Hall effect provides a powerful tool to guide chiral photon propagation on chip, which is essential to realize this form of optical information transmission. Chirality-dependent unidirectional photon propagation has been demonstrated in hybrid systems, which combine semiconductor quantum emitters and waveguides [131]. The chirality of the emitted photons is governed by the optical selection rules in the semiconductor QD. The direction of the photon propagation is controlled by a properly designed waveguide. Coles and coworkers demonstrated control of the direction of chiral photon emission by coupling a QD to a nonchiral waveguide (Figure 11C) [131]. When the QD is positioned at the center of the waveguide, the emission intensities are the same for both directions (Figure 11D) as expected from the symmetry consideration of the nonchiral waveguide. In contrast, when the QD is displaced from the center, the in-plane mirror symmetry of the hybrid system is broken. As a result, the emission direction depends on the chirality, with σ^+ photons preferentially propagating in one direction and σ^- photons in the other direction (Figure 11D). In another example [132], Sollner and coworkers demonstrated chirality-dependent directional emission of a QD by coupling it to a specially designed waveguide with broken mirror symmetry, known as a glide-plane waveguide, as shown in Figure 11E. When coupled to a glide-plane waveguide, an excited QD with σ polarization transition dipole preferentially emits photons in one direction (Figure 11F). When the chirality reverses, so does the emission direction.

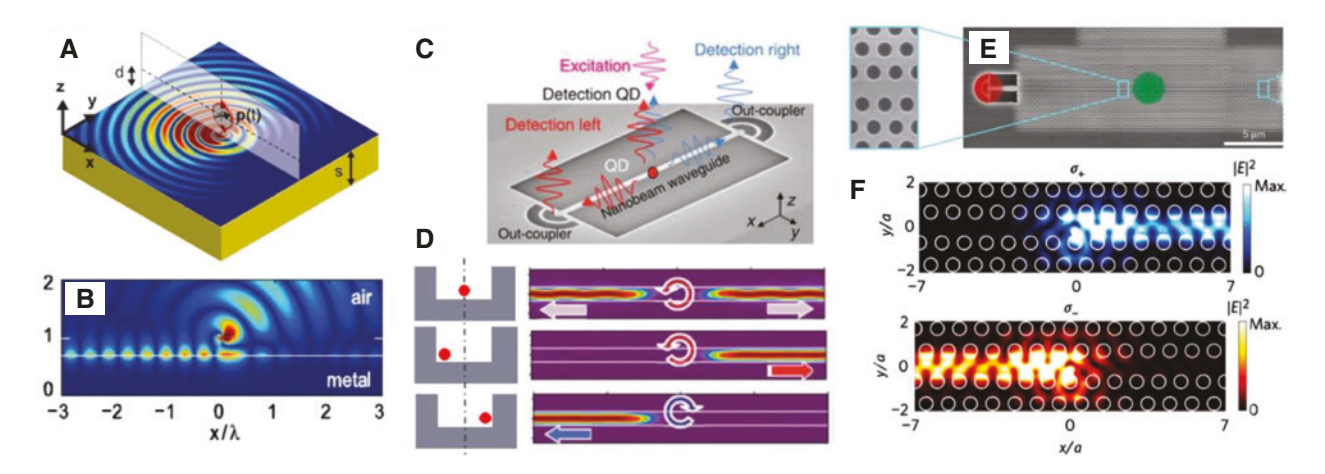


Figure 11: Chiral photonic structures and guiding chiral-dependent emission from semiconductor quantum dots using a specially designed waveguide.

(A) Schematic of the asymmetric excitation of SPPs from a circularly polarized dipole over a planar metal—dielectric interface. The dipole is in the xz-plane, which is perpendicular to the metal—dielectric interface. (B) Magnetic field distribution of the excited SPP mode by a 2D circularly polarized dipole over an air/metal interface. (C) Schematic of the directing chiral emission from a quantum dot coupled to a single-mode nanobeam waveguide. Red (blue) arrows represent the emission from right- (left-) circularly polarized optical dipoles of the quantum dot. (D) Calculated emission intensity with and without chirality dependent propagation, determined by the quantum dot position relative to the waveguide. (E) SEM image of the glide-plane waveguide. A quantum dot is optically excited in the center (green area) and the emission is detected at the out coupling grating (red area). The zoom-in SEM image shows the photonic crystal design of the shifted holes on the two sides. (F) Calculated directional emission from σ^+ and σ^- polarized dipoles in the glide-plane waveguide. Panel (A, B), (C, D), and (E, F) are adapted with permission from Ref. [130], The American Association for the Advancement of Science; Ref. [131], Nature Publishing Group; and Ref. [132], Nature Publishing Group; respectively.

Considering these examples of chirality-dependent photonic devices and the valley-contrasting optical selection rules in TMD monolayers, it is natural to extend these approaches to realize valleytronic devices. In such a hybrid system, TMD monolayers act as the active component while photonic structures function as the passive components. For example, the spatial separation of excitons with a specific valley index may be realized by routing valley excitons facilitated by the optical spin Hall effect. Chiral photons emitted by valley-polarized excitons may be channeled toward different directions. Below, we review two recent works exploring such opportunities.

4.3.2 Plasmonic nanowires

Nanowires can harvest exciton emission with exceptionally high efficiency as previous studies on coupling QDs and plasmonic wires have demonstrated [133, 134]. Taking advantage of this effect, a valley–photon interface has been realized by coupling a single silver nanowire to a few-layer-thick WS $_2$ flake (Figure 12A) [135]. The nanowire supports guided-SPPs possessing transverse optical spin angular momentum, which is locked with the propagation direction. The chirality-dependent directionality is illustrated in Figure 12B. A source positioned in the upper part

of the nanowire (y>0) and emitting light with $\sigma_{_+}(\sigma_{_-})$ polarization, will excite a SPP propagating to the left (right). The effect is inverted when the source is positioned in the lower part (y<0). Therefore, the chirality of the optical spin angular momentum is determined by a combination of the propagation direction and the y position.

Experimentally, valley-polarized excitons were locally excited in the middle of the silver nanowire (x=0) for different y positions with a circularly polarized laser of 594 nm. The K and K' valley excitons are associated with in-plane circularly polarized dipoles oscillating with opposite helicity $(E_x \pm i E_y)$ [136]. The transition dipoles from different valleys couple to the guided SPP modes propagating in opposite directions. The scattered PL at the end of the nanowire was detected on a charge-coupled device (CCD) after passing through a band-pass filter (620–630 nm), chosen to overlap with the exciton resonance in WS₂.

The valley-dependent directionality is quantified by $k_{\rm exp} \equiv [I_L(y) - I_R(y)]/[I_L(y) + I_R(y)]$, where $I_{L,R}(y)$ represent the PL intensity scattered at the left and right end of the nanowire as a function of y, as shown in Figure 12C, D. When the σ_- excitation spot is above (below) the nanowire, i.e. at y < 0 (y > 0), the excitons couple to SPPs propagating to left (right) end of the nanowire. When the handedness of the excitation is reversed, so does the

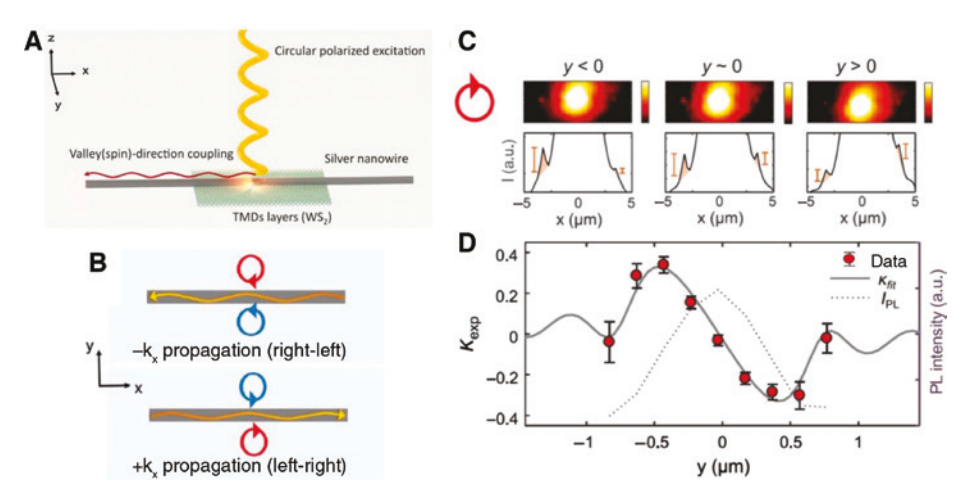


Figure 12: Coupling between valley-polarized excitons and guided SPPs in the WS, -nanowire hybrid structure. (A) Schematic of directional emission of valley-polarized excitons in the WS₂-nanowire hybrid structure. (B) Distribution of optical spin handedness depends on both the position and propagation direction. (C) PL spatial maps of valley-polarized excitons (top plots, in log scale) and line cuts along the nanowire (bottom plots, in linear scale) under left-circularly polarized optical excitation for three different excitation vertical positions. The intensity near the excitation spot is intentionally saturated for better contrast of the signal. (D) Directional coupling efficiency, defined as $k_{\text{ave}} = (l_i - l_i)/(l_i + l_i)$, measured for guided emission as a function of the position of the laser spot, with lefthanded circular polarization excitation. Gray line is the fitting result from the calculated directional coupling efficiency and the dotted line is the total PL intensity. Panels are adapted with permission from Ref. [135], The American Association for the Advancement of Science.

propagation direction. Note that the chirality-dependent propagation can only be achieved under asymmetric excitation condition in the transverse direction (i.e. $y \neq 0$) because of the symmetry of the nanowire. If the excitation laser spot is centered with respect to the nanowire (y=0), valley polarization separation vanishes. This sensitive dependence on the excitation position makes this scheme for spatial valley separation quite challenging for practical applications.

4.3.3 Metasurfaces

Metasurfaces with broken-mirror symmetry have been recently proposed to spatially separate valley excitons in TMDs at room temperature. The metasurface introduced in Ref. [137] consists of asymmetrical grooves arranged in a sub-wavelength period. Figure 13F shows the SEM image of the cross-section of the fabricated asymmetric grooves. In the case of symmetric grooves (Figure 13A), the mirror symmetry along the yz-plane leads to chiralityindependent propagation, i.e. an in-plane dipole with left- or right-handed chirality couples to both sidewalls equally, similarly to the symmetric nanowire considered above. However, when the mirror symmetry is intentionally broken by tilting one side wall while keeping the other wall vertical, the guided SPPs (gSPPs) excited by valley exciton dipoles are different for vertical and tilted walls (Figure 13B), resulting in chirality-dependent, unidirectional propagation of gSPPs.

Experimentally, a linearly polarized laser at wavelength 532 nm was used to equally populate the two valleys in the monolayer MoS, placed on top of the metasurface. The valley-excitons then induced chiral gSPPs propagating away from the laser excitation spot and reexcited excitons along its path. Such exciton-gSPP-exciton nonradiative energy transfer process separated the valley excitons spatially, as shown in Figure 13H, I. The g-SPP modes have an E-field with a significant in-plane component. Thus, the coupling between the in-plane dipoles associated with excitons in monolayer TMD and gSPPs can be rather efficient. The efficiency of the cascaded energy conversion process of the exciton-gSPPexciton is calculated to be higher than 20%. In a control experiment, the researchers showed that such spatial valley separation was absent when the MoS, monolayer was placed on a metasurface consisting of symmetric grooves (Figure 13J). The asymmetric metasurface can also direct valley exciton emission to different directions, serving as an interface between valleytronics and photonic devices similar to those discussed in earlier in this section.

The two examples chosen in this section have demonstrated that plasmonic antennas and metasurfaces can be used to control the valley index including the degree of valley polarization, the emission direction of

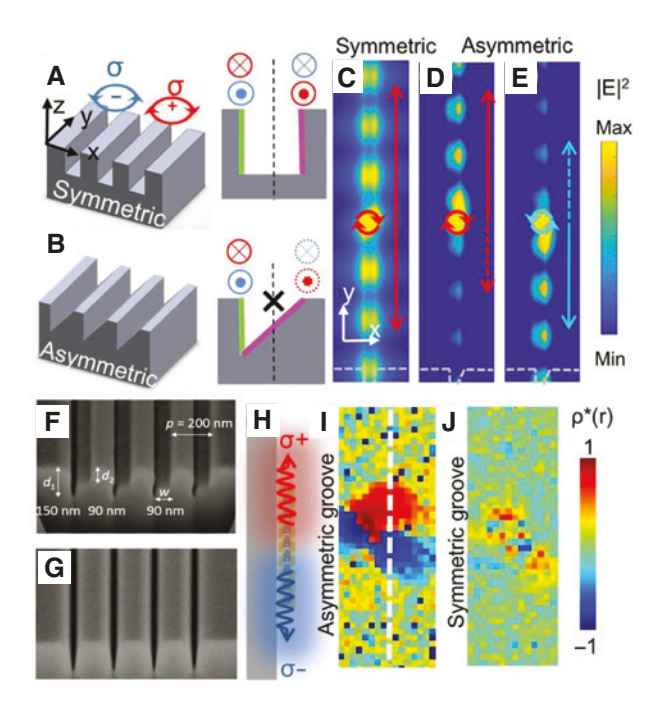


Figure 13: Spatial separation of valley excitons in a MoS₂ monolayer-Ag metasurface hybrid system.

Schematic of the propagating directions of guided SPPs launched by σ^+ and σ^- dipoles in (A) symmetric and (B) asymmetric groove arrays. The gSPPs excited by σ^+ (σ^-) dipoles propagate into (out of) the panel on the left wall, and the direction is revered on the right wall. (C) Calculated electric field distributions excited by a σ^- dipole on a symmetric groove array show no chirality-dependent SPP propagation due to the mirror symmetry. (D, E) Calculated electric field distributions excited by σ^- and σ^+ dipole on the asymmetric grating, respectively. Gray dashed lines in the bottom indicate the position of a groove. (F, G) SEM images of the asymmetric and symmetric grooves. (H) Schematic of valley-excitons spatially separated by the metasurface. Color map of valley polarization contrast $\rho(r)$ from a MoS $_2$ monolayer coupled to (I) asymmetric and (J) symmetric groove arrays. Panels are adapted with permission from Ref. [137], Nature Publishing Group.

valley polarized excitons, and the spatial separation of valley excitons. The performance of these hybrid photonic devices is determined by SPP propagation, ultrafast exciton dynamics, and how plasmonic nanostructures modify such dynamics via exciton–plasmon coupling. Because of the large oscillator strength of valley excitons in TMDs, a strong coupling between valley excitons and SPPs or LSRPs can be reached in properly designed plasmonic structures.

5 Outlook

TMDs represent a new class of flexible photonic materials, hosting single-photon emitters with defined locations

and extending optical control to a new quantum degree of freedom, the valley. Integrating these layered materials with plasmonic nanostructures, waveguides, and metasurfaces advances both classical and quantum photonics. There are a few clear future directions in this field of research. Proper waveguides that can guide single-photon emission efficiently and preserve the polarization states, which are often used to encode quantum information of flying qubits, have yet to be demonstrated. Addressing the long-standing challenge of loss in plasmonic materials will improve the performance of hybrid photonic devices. For example, the limited degree of valley polarization in the hybrid system can be improved by implementing new metasurface designs that can specifically couple to dark exciton states or reduce the energy concentration in noble metals.

With the rapid progress in synthesizing and fabricating van der Waals (vdW) heterostructures, new exciton resonances are identified. The interlayer excitons in vdW heterostructures exhibit long recombination and valley polarization times [138–143]. The long recombination lifetime suggests that their oscillator strength is small and couples relatively weakly to light. Such slow dynamics may also be related to indirect transitions in the momentum space. Plasmonic nanostructures placed near TMD heterostructures may lead to measurable changes in exciton dynamics by shaping the photon density of states and provide coupling to large photon momenta in the near field to brighten indirect transitions. Plasmonic nanostructures may provide a strong field enhancement, needed for optical switching of topological phases of matter [144-146]. A metasurface may further define the optical properties of an array of identical single-photon emitters localized by an in-plane Moiré superlattice [147, 148].

Acknowledgments: LS was supported by NSF DMR-1306878, Funder Id: http://dx.doi.org/10.13039/100000078. JC was partially supported by the NSF MRSEC program DMR-1720595, Funder Id: http://dx.doi.org/10.13039/100000078, Grant Number: NSF DMR-1808042, which also facilitated the collaboration between XL and AA. XL acknowledges the support from the Welch Foundation via grant F-1662, Funder Id: http://dx.doi.org/10.13039/100000928. AA and MC acknowledge the Air Force Office of Scientific Research with MURI grant No. FA9550-17-1-0002, Funder Id:http://dx.doi.org/10.13039/10000181 and the Welch Foundation with grant No. F-1802, Funder Id:http://dx.doi.org/10.13039/100000928. MC was supported by a Rubicon postdoctoral fellowship by The Netherlands Organization for Scientific Research (NWO).

References

- [1] Novoselov KS, Mishchenko A, Carvalho A, Castro Neto AH. 2D materials and van der Waals heterostructures. Science 2016;353:aac9439.
- [2] Geim AK. Nobel lecture: random walk to graphene. Rev Mod Phys 2011;83:851-62.
- [3] Britnell L, Ribeiro RM, Eckmann A, et al. Strong light-matter interactions in heterostructures of atomically thin films. Science 2013;340:1311-4.
- [4] Mak KF, Xiao D, Shan J. Light-valley interactions in 2D semiconductors. Nat Photonics 2018;12:451-60.
- [5] Malic E, Selig M, Feierabend M, et al. Dark excitons in transition metal dichalcogenides. Phys Rev Mater 2018;2:014002.
- [6] Baranowski M, Surrente A, Maude DK, et al. Dark excitons and the elusive valley polarization in transition metal dichalcogenides. 2D Mater 2017;4:025016.
- [7] Hsu W-T, Lu L-S, Wang D, et al. Evidence of indirect gap in monolayer WSe₃. Nat Commun 2017;8:929.
- [8] Zhang C, Chen Y, Johnson A, et al. Probing critical point energies of transition metal dichalcogenides: surprising indirect gap of single layer WSe₂. Nano Lett 2015;15:6494-500.
- [9] Mak KF, Lee C, Hone J, Shan J, Heinz TF. Atomically thin MoS,: a new direct-gap semiconductor. Phys Rev Lett 2010;105:136805.
- [10] Splendiani A, Sun L, Zhang Y, et al. Emerging photoluminescence in monolayer MoS₂. Nano Lett 2010;10:1271-5.
- [11] Jin W, Yeh PC, Zaki N, et al. Direct measurement of the thickness-dependent electronic band structure of MoS, using angle-resolved photoemission spectroscopy. Phys Rev Lett 2013:111:106801.
- [12] Mak KF, He K, Lee C, et al. Tightly bound trions in monolayer MoS₃. Nat Mater 2013;12:207.
- [13] Ross JS, Wu S, Yu H, et al. Electrical control of neutral and charged excitons in a monolayer semiconductor. Nat Commun 2013;4:1474.
- [14] Berkelbach TC, Hybertsen MS, Reichman DR. Theory of neutral and charged excitons in monolayer transition metal dichalcogenides. Phys Rev B 2013;88:045318.
- [15] Lui C, Frenzel AJ, Pilon DV, et al. Trion-induced negative photoconductivity in monolayer MoS₂. Phys Rev Lett 2014;113:166801.
- [16] Singh A, Moody G, Tran K, et al. Trion formation dynamics in monolayer transition metal dichalcogenides. Phys Rev B 2016;93:041401.
- [17] Krasnok A, Lepeshov S, Alu A. Nanophotonics with 2D transition metal dichalcogenides [Invited]. Opt Express 2018;26:15972-94.
- [18] Srivastava A, Sidler M, Allain AV, et al. Optically active quantum dots in monolayer WSe₃. Nat Nanotechnol 2015;10:491-6.
- [19] He Y-M, Clark G, Schaibley JR, et al. Single quantum emitters in monolayer semiconductors. Nat Nanotechnol 2015;10:497-502.
- [20] Chakraborty C, Kinnischtzke L, Goodfellow KM, Beams R, Vamivakas AN. Voltage-controlled quantum light from an atomically thin semiconductor. Nat Nanotechnol 2015;10:507-11.
- [21] Mak KF, He K, Shan J, Heinz TF. Control of valley polarization in monolayer MoS, by optical helicity. Nat Nanotechnol 2012;7:494-8.
- [22] Zeng H, Dai J, Yao W, Xiao D, Cui X. Valley polarization in MoS, monolayers by optical pumping. Nat Nanotechnol 2012;7:490-3.

- [23] Cao T, Wang G, Han W, et al. Valley-selective circular dichroism of monolayer molybdenum disulphide. Nat Commun 2012;3:887.
- [24] Kim H, Ahn GH, Cho J, et al. Synthetic WSe, monolayers with high photoluminescence quantum yield. Sci Adv 2019;5:eaau4728.
- [25] Edelberg D, Rhodes D, Kerelsky A, et al. Hundredfold enhancement of light emission via defect control in monolayer transition-metal dichalcogenides. arXiv preprint arXiv:1805.00127:2018.
- [26] Schneider C, Glazov MM, Korn T, Hofling S, Urbaszek B. Twodimensional semiconductors in the regime of strong lightmatter coupling. Nat Commun 2018;9:2695.
- [27] Stier AV, Wilson NP, Clark G, Xu X, Crooker SA. Probing the influence of dielectric environment on excitons in monolayer WSe3: insight from high magnetic fields. Nano Lett 2016;16:7054-60.
- [28] Wang G, Chernikov A, Glazov MM, et al. Colloquium: excitons in atomically thin transition metal dichalcogenides. Rev Mod Phys 2018;90:021001.
- [29] Chernikov A, Berkelbach TC, Hill HM, et al. Exciton binding energy and nonhydrogenic rydberg series in monolayer WS₂. Phys Rev Lett 2014;113:076802.
- [30] Hanbicki AT, Currie M, Kioseoglou G, Friedman AL, Jonker BT. Measurement of high exciton binding energy in the monolayer transition-metal dichalcogenides WS, and WSe,. Solid State Commun 2015;203:16-20.
- Zhu B, Chen X, Cui X. Exciton binding energy of monolayer WS₂. Sci Rep 2015;5:9218.
- [32] He K, Kumar N, Zhao L, et al. Tightly bound excitons in monolayer WSe₃. Phys Rev Lett 2014;113:026803.
- [33] Miller RC, Kleinman DA, Tsang WT, Gossard AC. Observation of the excited level of excitons in GaAs quantum wells. Phys Rev B 1981:24:1134-6.
- [34] Greene RL, Bajaj KK, Phelps DE. Energy levels of Wannier excitons in GaAs – Ga, Al, As quantum-well structures. Phys Rev B 1984;29:1807-12.
- [35] Ugeda MM, Bradley AJ, Shi S-F, et al. Giant bandgap renormalization and excitonic effects in a monolayer transition metal dichalcogenide semiconductor. Nat Mater 2014;13:1091.
- [36] Wang G, Marie X, Gerber I, et al. Giant enhancement of the optical second-harmonic emission of WSe, monolayers by laser excitation at exciton resonances. Phys Rev Lett 2015;114:097403.
- [37] Qiu DY, da Jornada FH, Louie SG. Optical spectrum of MoS₂: many-body effects and diversity of exciton states. Phys Rev Lett 2013;111:216805.
- [38] Berghäuser G, Malic E. Analytical approach to excitonic properties of MoS₂. Phys Rev B 2014;89:125309.
- [39] Hao K, Specht JF, Nagler P, et al. Neutral and charged inter-valley biexcitons in monolayer MoSe₂. Nat Commun 2017;8:15552.
- [40] Ye Z, Waldecker L, Ma EY, et al. Efficient generation of neutral and charged biexcitons in encapsulated WSe, monolayers. Nat Commun 2018;9:3718.
- [41] Mak KF, Shan J. Photonics and optoelectronics of 2D semiconductor transition metal dichalcogenides. Nat Photonics 2016;10:216-26.
- [42] Wang QH, Kalantar-Zadeh K, Kis A, Coleman JN, Strano MS. Electronics and optoelectronics of two-dimensional transition metal dichalcogenides. Nat Nanotechnol 2012;7:699-712.

- [43] Liu X, Galfsky T, Sun Z, et al. Strong light-matter coupling in two-dimensional atomic crystals. Nat Photonics 2014;9:30-4.
- [44] Fogler MM, Butov LV, Novoselov KS. High-temperature superfluidity with indirect excitons in van der Waals heterostructures. Nat Commun 2014;5:4555.
- [45] Wang H, Zhang C, Chan W, Manolatou C, Tiwari S, Rana F. Radiative lifetimes of excitons and trions in monolayers of the metal dichalcogenide MoS₂. Phys Rev B 2016;93:045407.
- [46] Palummo M, Bernardi M, Grossman JC. Exciton radiative lifetimes in two-dimensional transition metal dichalcogenides. Nano Lett 2015;15:2794-800.
- [47] Sun D, Rao Y, Reider GA, et al. Observation of rapid excitonexciton annihilation in monolayer molybdenum disulfide. Nano Lett 2014;14:5625-9.
- [48] Kumar N, Cui Q, Ceballos F, He D, Wang Y, Zhao H. Excitonexciton annihilation in MoSe, monolayers. Phys Rev B 2014;89:125427.
- [49] Mouri S, Miyauchi Y, Toh M, Zhao W, Eda G, Matsuda K. Nonlinear photoluminescence in atomically thin layered WSe, arising from diffusion-assisted exciton-exciton annihilation. Phys Rev B 2014;90:155449.
- [50] Robert C, Lagarde D, Cadiz F, et al. Exciton radiative lifetime in transition metal dichalcogenide monolayers. Phys Rev B 2016:93:205423.
- [51] Moody G, Dass CK, Hao K, et al. Intrinsic homogeneous linewidth and broadening mechanisms of excitons in monolayer transition metal dichalcogenides. Nat Commun 2015;6:8315.
- [52] Jakubczyk T, Delmonte V, Koperski M, et al. Radiatively limited dephasing and exciton dynamics in MoSe, monolayers revealed with four-wave mixing microscopy. Nano Lett 2016;16:5333-9.
- [53] Jin C, Kim J, Wu K, et al. On optical dipole moment and radiative recombination lifetime of excitons in WSe₃. Adv Funct Mater 2017;27:1601741.
- [54] Shi H, Yan R, Bertolazzi S, et al. Exciton dynamics in suspended monolayer and few-layer MoS₂ 2D crystals. ACS Nano 2013;7:1072-80.
- [55] Kleemann M-E, Chikkaraddy R, Alexeev EM, et al. Strongcoupling of WSe, in ultra-compact plasmonic nanocavities at room temperature. Nat Commun 2017;8:1296.
- [56] Stührenberg M, Munkhbat B, Baranov DG, et al. Strong light-matter coupling between plasmons in individual gold Bipyramids and excitons in mono- and multilayer WSe₂. Nano Lett 2018;18:5938-45.
- [57] Koperski M, Nogajewski K, Arora A, et al. Single photon emitters in exfoliated WSe, structures. Nat Nanotechnol 2015:10:503-6.
- [58] Tonndorf P, Schmidt R, Schneider R, et al. Single-photon emission from localized excitons in an atomically thin semiconductor. Optica 2015;2:347-52.
- [59] Palacios-Berraquero C, Kara DM, Montblanch AR-P, et al. Large-scale quantum-emitter arrays in atomically thin semiconductors. Nat Commun 2017;8:15093.
- [60] Lodahl P, Mahmoodian S, Stobbe S. Interfacing single photons and single quantum dots with photonic nanostructures. Rev Mod Phys 2015;87:347.
- [61] Iff O, Lundt N, Betzold S, et al. Deterministic coupling of quantum emitters in WSe, monolayers to plasmonic nanocavities. Opt Express 2018;26:25944-51.

- [62] Tripathi LN, Iff O, Betzold S, et al. Spontaneous emission enhancement in strain-induced WSe, monolayer-based quantum light sources on metallic surfaces. ACS Photonics 2018;5:1919-26.
- [63] Xu X, Yao W, Xiao D, Heinz TF. Spin and pseudospins in layered transition metal dichalcogenides. Nat Phys 2014;10:343-50.
- [64] Xiao D, Liu G-B, Feng W, Xu X, Yao W. Coupled spin and valley physics in monolayers of MoS, and other group-VI dichalcogenides. Phys Rev Lett 2012;108:196802.
- [65] Schaibley JR, Yu H, Clark G, et al. Valleytronics in 2D materials. Nat Rev Mater 2016;1:16055.
- [66] Gunawan O, Shkolnikov YP, Vakili K, Gokmen T, De Poortere EP, Shayegan M. Valley susceptibility of an interacting two-dimensional electron system. Phys Rev Lett 2006:97:186404.
- [67] Shkolnikov Y, De Poortere E, Tutuc E, Shayegan M. Valley splitting of AlAs two-dimensional electrons in a perpendicular magnetic field. Phys Rev Lett 2002;89:226805.
- [68] Rycerz A, Tworzydło J, Beenakker C. Valley filter and valley valve in graphene. Nat Phys 2007;3:172-5.
- [69] Jha PK, Shitrit N, Ren X, Wang Y, Zhang X. Spontaneous exciton valley coherence in transition metal dichalcogenide monolayers interfaced with an anisotropic metasurface. Phys Rev Lett 2018:121:116102.
- [70] Sallen G, Bouet L, Marie X, et al. Robust optical emission polarization in MoS, monolayers through selective valley excitation. Phys Rev B 2012;86:081301.
- [71] Bellus MZ, Ceballos F, Chiu H-Y, Zhao H. Tightly bound trions in transition metal dichalcogenide heterostructures. ACS Nano 2015;9:6459-64.
- [72] Mouri S, Miyauchi Y, Matsuda K. Tunable photoluminescence of monolayer MoS, via chemical doping. Nano Lett 2013;13:5944-8.
- [73] Rivera P, Schaibley JR, Jones AM, et al. Observation of longlived interlayer excitons in monolayer MoSe, -WSe, heterostructures. Nat Commun 2015;6:6242.
- [74] Singh A, Tran K, Kolarczik M, et al. Long-lived valley polarization of intravalley trions in monolayer WSe₃. Phys Rev Lett 2016;117:257402.
- [75] Song X, Xie S, Kang K, Park J, Sih V. Long-lived hole spin/valley polarization probed by Kerr rotation in monolayer WSe₂. Nano Lett 2016;16:5010-4.
- [76] Hao K, Moody G, Wu F, et al. Direct measurement of exciton valley coherence in monolayer WSe₃. Nat Phys 2016;12:677-
- [77] Plechinger G, Korn T, Lupton JM. Valley-polarized exciton dynamics in exfoliated monolayer WSe₂. J Phys Chem C 2017:121:6409-13.
- [78] Poellmann C, Steinleitner P, Leierseder U, et al. Resonant internal quantum transitions and femtosecond radiative decay of excitons in monolayer WSe₂. Nat Mater 2015;14:889-93.
- [79] O'brien JL, Furusawa A, Vučković J. Photonic quantum technologies. Nat Photonics 2009;3:687-95.
- [80] Arcari M, Söllner I, Javadi A, et al. Near-unity coupling efficiency of a quantum emitter to a photonic crystal waveguide. Phys Rev Lett 2014;113:093603.
- [81] Ding X, He Y, Duan Z-C, et al. On-demand single photons with high extraction efficiency and near-unity indistinguishability from a resonantly driven quantum dot in a micropillar. Phys Rev Lett 2016:116:020401.

- [82] Somaschi N, Giesz V, De Santis L, et al. Near-optimal singlephoton sources in the solid state. Nat Photonics 2016;10:340-5.
- [83] Novotny L, Hecht B. Principles of nano-optics. Cambridge, UK, Cambridge University Press, 2012.
- [84] Cai T, Kim J-H, Yang Z, Dutta S, Aghaeimeibodi S, Waks E. Radiative enhancement of single quantum emitters in WSe, monolayers using site-controlled metallic nanopillars. ACS Photonics 2018;5:3466-71.
- [85] Luo Y, Shepard GD, Ardelean JV, et al. Deterministic coupling of site-controlled quantum emitters in monolayer WSe, to plasmonic nanocavities. Nat Nanotechnol 2018;13:1137-42.
- [86] Russell KJ, Liu T-L, Cui S, Hu EL. Large spontaneous emission enhancement in plasmonic nanocavities. Nat Photonics 2012:6:459-62.
- [87] Hu S, Khater M, Salas-Montiel R, et al. Experimental realization of deep-subwavelength confinement in dielectric optical resonators. Sci Adv 2018;4:eaat2355.
- [88] Robinson JT, Manolatou C, Chen L, Lipson M. Ultrasmall mode volumes in dielectric optical microcavities. Phys Rev Lett 2005;95:143901.
- [89] Hu S, Weiss SM. Design of photonic crystal cavities for extreme light concentration. ACS Photonics 2016;3:1647-
- [90] Choi H, Heuck M, Englund D. Self-similar nanocavity design with ultrasmall mode volume for single-photon nonlinearities. Phys Rev Lett 2017;118:223605.
- [91] Koenderink AF. On the use of Purcell factors for plasmon antennas. Opt Lett 2010;35:4208-10.
- [92] Sauvan C, Hugonin J-P, Maksymov I, Lalanne P. Theory of the spontaneous optical emission of nanosize photonic and plasmon resonators. Phys Rev Lett 2013;110:237401.
- [93] Kristensen PT, Hughes S. Modes and mode volumes of leaky optical cavities and plasmonic nanoresonators. ACS Photonics 2014;1:2-10.
- [94] Koenderink AF. Single-photon nanoantennas. ACS Photonics 2017;4:710-22.
- [95] Novotny L, Van Hulst N. Antennas for light. Nat Photonics
- [96] Alù A, Engheta N. Tuning the scattering response of optical nanoantennas with nanocircuit loads. Nat Photonics 2008;2:307-10.
- [97] Monticone F, Argyropoulos C, Alu A. Optical antennas: controlling electromagnetic scattering, radiation, and emission at the nanoscale. IEEE Antennas Propag Mag 2017;59:43-61.
- [98] Kuttge M, García de Abajo FJ, Polman A. Ultrasmall mode volume plasmonic nanodisk resonators. Nano Lett 2009;10:1537-41.
- [99] Akselrod GM, Argyropoulos C, Hoang TB, et al. Probing the mechanisms of large Purcell enhancement in plasmonic nanoantennas. Nat Photonics 2014;8:835-40.
- [100] Wang C, Badolato A, Wilson-Raea I, Petroff PM, Hu E. Optical properties of single InAs quantum dots in close proximity to surfaces. Appl Phys Lett 2004;85:3423-5.
- [101] Zhang H, Huo Y, Lindfors K, et al. Narrow-line self-assembled GaAs quantum dots for plasmonics. Appl Phys Lett 2015;106:101110.
- [102] Farahani JN, Pohl DW, Eisler H-J, Hecht B. Single quantum dot coupled to a scanning optical antenna: a tunable superemitter. Phys Rev Lett 2005;95:017402.

- [103] Lyamkina A, Schraml K, Regler A, et al. Monolithically integrated single quantum dots coupled to bowtie nanoantennas. Opt Express 2016;24:28936-44.
- [104] Pfeiffer M, Lindfors K, Zhang H, et al. Eleven nanometer alignment precision of a plasmonic nanoantenna with a selfassembled GaAs quantum dot. Nano Lett 2013;14:197-201.
- [105] Regler A, Schraml K, Lyamkina A, et al. Emission redistribution from a quantum dot-bowtie nanoantenna. J Nanophotonics 2016:10:033509.
- [106] Lee B, Park J, Han GH, et al. Fano resonance and spectrally modified photoluminescence enhancement in monolayer MoS, integrated with plasmonic nanoantenna array. Nano Lett 2015;15:3646-53.
- [107] Butun S, Tongay S, Aydin K. Enhanced light emission from large-area monolayer MoS, using plasmonic nanodisc arrays. Nano Lett 2015;15:2700-4.
- [108] Johnson AD, Cheng F, Tsai Y, Shih CK. Giant enhancement of defect-bound exciton luminescence and suppression of bandedge luminescence in monolayer WSe,-Ag plasmonic hybrid structures. Nano Lett 2017;17:4317-22.
- [109] Eggleston MS, Desai SB, Messer K, et al. Ultrafast spontaneous emission from a slot-antenna coupled WSe, monolayer. ACS Photonics 2018;5:2701-5.
- [110] Dutta S, Cai T, Buyukkaya MA, Barik S, Aghaeimeibodi S, Waks E. Coupling quantum emitters in WSe, monolayers to a metalinsulator-metal waveguide. Appl Phys Lett 2018;113:191105.
- [111] Palacios E, Park S, Butun S, Lauhon L, Aydin K. Enhanced radiative emission from monolayer MoS, films using a single plasmonic dimer nanoantenna. Appl Phys Lett 2017;111:031101.
- [112] Cai T, Dutta S, Aghaeimeibodi S, et al. Coupling emission from single localized defects in two-dimensional semiconductor to surface plasmon polaritons. Nano Lett 2017;17:6564-8.
- [113] Amani M, Lien D-H, Daisuke Kiriya D, et al. Near-unity photoluminescence quantum yield in MoS₂. Science 2015;350:1065-8.
- [114] Li Z, Liu C, Rong X, et al. Tailoring MoS, valley-polarized photoluminescence with super chiral near-field. Adv Mater 2018;30:1801908.
- [115] Chervy T, Azzini S, Lorchat E, et al. Room temperature chiral coupling of valley excitons with spin-momentum locked surface plasmons. ACS Photonics 2018;5:1281-7.
- [116] Chen H, Liu M, Xu L, Neshev DN. Valley-selective directional emission from a transition-metal dichalcogenide monolayer mediated by a plasmonic nanoantenna. Beilstein J Nanotechnol 2018;9:780-8.
- [117] Reithmaier JP, Sęk G, Löffler A, et al. Strong coupling in a single quantum dot-semiconductor microcavity system. Nature 2004;432:197-200.
- [118] Dintinger J, Klein S, Bustos F, Barnes WL, Ebbesen T. Strong coupling between surface plasmon-polaritons and organic molecules in subwavelength hole arrays. Phys Rev B 2005;71:035424.
- [119] Ezawa M. Valley-polarized metals and quantum anomalous Hall effect in silicene. Phys Rev Lett 2012;109:055502.
- [120] Tahir M, Manchon A, Sabeeh K, Schwingenschlögl U. Quantum spin/valley Hall effect and topological insulator phase transitions in silicene. Appl Phys Lett 2013;102:162412.
- [121] Lee J, Mak KF, Shan J. Electrical control of the valley Hall effect in bilayer MoS, transistors. Nat Nanotechnol 2016;11:421-5.
- [122] Guinea F, Katsnelson M, Geim A. Energy gaps and a zero-field quantum Hall effect in graphene by strain engineering. Nat Phys 2010;6:30-3.

- [123] Zhang Y, Tan Y-W, Stormer HL, Kim P. Experimental observation of the quantum Hall effect and Berry's phase in graphene. Nature 2005;438:201-4.
- [124] Mak KF, McGill KL, Park J, McEuen PL. The valley Hall effect in MoS, transistors. Science 2014;344:1489-92.
- [125] Onga M, Zhang Y, Ideue T, Iwasa Y. Exciton Hall effect in monolayer MoS₂. Nat Mater 2017;16:1193.
- [126] Petersen J, Volz J, Rauschenbeutel A. Chiral nanophotonic waveguide interface based on spin-orbit interaction of light. Science 2014;346:67-71.
- [127] Kavokin A, Malpuech G, Glazov M. Optical spin Hall effect. Phys Rev Lett 2005;95:136601.
- [128] Leyder C, Romanelli M, Karr JP, et al. Observation of the optical spin Hall effect. Nat Phys 2007;3:628-31.
- [129] Mueller JPB, Capasso F. Asymmetric surface plasmon polariton emission by a dipole emitter near a metal surface. Phys Rev B 2013;88:121410.
- [130] Rodríguez-Fortuño FJ, Marino G, Ginzburg P, et al. Near-field interference for the unidirectional excitation of electromagnetic guided modes. Science 2013;340:328-30.
- [131] Coles RJ, Price DM, Dixon JE, et al. Chirality of nanophotonic waveguide with embedded quantum emitter for unidirectional spin transfer. Nat Commun 2016;7:11183.
- [132] Sollner I, Mahmoodian S, Hansen SL, et al. Deterministic photon-emitter coupling in chiral photonic circuits. Nat Nanotechnol 2015;10:775-8.
- [133] Wei H, Ratchford D, Li X, Xu H, Shih C-K. Propagating surface plasmon induced photon emission from quantum dots. Nano Lett 2009;9:4168-71.
- [134] Akimov AV, Mukherjee A, Yu CL, et al. Generation of single optical plasmons in metallic nanowires coupled to quantum dots. Nature 2007;450:402-6.
- [135] Gong S-H, Alpeggiani F, Sciacca B, Garnett EC, Kuipers L. Nanoscale chiral valley-photon interface through optical spinorbit coupling. Science 2018;359:443-7.
- [136] Schuller JA, Karaveli S, Schiros T, et al. Orientation of luminescent excitons in layered nanomaterials. Nat Nanotechnol 2013;8:271-6.

- [137] Sun L, Wang C-Y, Krasnok A, et al. Separation of valley excitons in a MoS, monolayer using a subwavelength asymmetric groove array. Nat Photonics 2019;13:180-4.
- [138] Hong X, Kim J, Shi S-F, et al. Ultrafast charge transfer in atomically thin MoS₂/WS₂ heterostructures. Nat Nanotechnol 2014;9:682-6.
- [139] Kozawa D, Carvalho A, Verzhbitskiy I, et al. Evidence for fast interlayer energy transfer in MoSe₂/WS₂ heterostructures. Nano Lett 2016:16:4087-93.
- [140] Chen H, Wen X, Zhang J, et al. Ultrafast formation of interlayer hot excitons in atomically thin MoS₂/WS₂ heterostructures. Nat Commun 2016;7:12512.
- [141] He J, Kumar N, Bellus KZ, et al. Electron transfer and coupling in graphene-tungsten disulfide van der Waals heterostructures. Nat Commun 2014:5:5622.
- [142] Ceballos F, Bellus MZ, Chiu H-Y, Zhao H. Ultrafast charge separation and indirect exciton formation in a MoS₂-MoSe₂ van der Waals heterostructure. ACS Nano 2014;8:12717-24.
- [143] Chiu M-H, Zhang C, Shiu H-W, et al. Determination of band alignment in the single-layer MoS₂/WSe₂ heterojunction. Nat Commun 2015;6:7666.
- [144] Claassen M, Jia C, Moritz B, Devereaux TP. All-optical materials design of chiral edge modes in transition-metal dichalcogenides. Nat Commun 2016;7:13074.
- [145] Iadecola T, Campbell D, Chamon C, et al. Materials design from nonequilibrium steady states: driven graphene as a tunable semiconductor with topological properties. Phys Rev Lett 2013;110:176603.
- [146] Perez-Piskunow PM, Usaj G, Balseiro CA, Foa Torres LEF. Floquet chiral edge states in graphene. Phys Rev B 2014;89:121401.
- [147] Yu H, Liu G-B, Tang J, Xu X, Yao W. Moiré excitons: from programmable quantum emitter arrays to spin-orbit-coupled artificial lattices. Sci Adv 2017;3:e1701696.
- [148] Wu F, Lovorn T, MacDonald AH. Theory of optical absorption by interlayer excitons in transition metal dichalcogenide heterobilayers. Phys Rev B 2018;97:035306.